

Quantification of soil structural heterogeneity and its impact on flow and transport

Dissertation

zur Erlangung des akademischen Grades

Dr. rer. nat.

vorgelegt der

Naturwissenschaftlichen Fakultät III der
Martin-Luther-Universität Halle-Wittenberg
Institut für Geowissenschaften und Geographie

von

Herr Dipl.-Geogr. Steffen Schlüter
geboren am 23.03.1983 in Schlema

Datum der Einreichung: 27.02.2012

Datum der Verteidigung: 19.07.2012

Gutachter: Prof. Dr. Hans-Jörg Vogel

Prof. Dr. Bernd Huwe

Abstract

Flow and transport in the subsurface are determined by the structural heterogeneity of natural porous media. Connectivity is known to be an important facet of structural heterogeneity that has to be captured adequately in order to facilitate or improve model predictions on diverse physical processes in porous formations. Connectivity is a broad concept that can be either understood as a structural property of a domain that describes the existence of a path for flow and transport from one location to another or as a functional property of a domain with respect to effective hydraulic behavior.

This thesis presents some novel insights into the approaches to quantify structural connectivity and the complex relationship between structural and functional connectivity in the realm of vadose zone hydrology. The central question to be addressed is, whether structural complexity can be reduced to some meaningful connectivity metrics that facilitate the prediction of effective hydraulic behavior. To this end, some well-established reference heterogeneity models with distinct differences in structural connectivity are introduced. Various structural connectivity metrics are surveyed by their capability to capture morphological differences between the reference models. This comprises metrics like the autocovariance function, Minkowski functions, chord length distributions, local percolation probability and the pair connectivity function. By means of the stochastic reconstruction paradigm it is demonstrated that a combined multi-point statistics including Minkowski functions and chord length distribution is able to reproduce structural connectivity with low computational effort.

The reference heterogeneity models and their stochastically reconstructed counterparts are then compared in terms of functional connectivity for different processes and states. This comprises two-dimensional numerical experiments on stationary single-phase flow, transport of a conservative tracer and hydraulic non-equilibrium during infiltration into an unsaturated soil. Functional connectivity metrics for each investigated process will be introduced, that all relate the effective behavior to some expectation value derived from the underlying parameter field. In order to do so, effective non-equilibrium is introduced as a novel concept that quantifies the decoupling of averaged

water content and matric potential at the infiltration front caused by preferential flow. A critical question is how to define averaged, transient state variables at the larger scale. Flux-weighted averaging of soil matric potential is especially suited in this regard, since it conserves hydraulic non-equilibrium during upscaling. Thus, effective hydraulic non-equilibrium is determined by the difference between dynamic and equilibrium water retention and can be interpreted towards the energy dissipation due to funneling of water into preferential flow paths.

It is demonstrated that a good reproduction of structural connectivity also entails a good reproduction of functional connectivity metrics. Thus, the investigated multi-point statistics carry some predictive power of effective hydraulic behavior. However, structural connectivity affect upscaled flow, transport and hydraulic non-equilibrium behavior differently. Flow connectivity is more sensitive to the continuity of highly conductive paths, whereas transport connectivity is more affected by the morphology of the flux pattern. Hydraulic non-equilibrium, in turn, depends on a delicate balance between vertical and lateral flux components. Thus, functional connectivity has to be considered as a process and state-dependent concept.

keywords: connectivity metrics, stochastic reconstruction, stationary flow, solute transport, hydraulic non-equilibrium, upscaling

Zusammenfassung

Fluss und Transport in natürlichen porösen Medien werden durch die Strukturheterogenität des Untergrunds bestimmt. Konnektivität ist ein wichtiger Aspekt jener Strukturheterogenität, welcher richtig erfasst werden muss, um Modelvorhersagen zu verschiedenen physikalischen Prozessen in porösen Medien zu ermöglichen oder zu verbessern. Konnektivität ist ein breit gefasster Begriff, der entweder als Struktureigenschaft eines Raumes aufgefasst werden kann, welche die Existenz eines Pfades für Fluss und Transport beschreibt, oder als funktionale Eigenschaft bezogen auf das effektive hydraulische Verhalten eines Raumes.

Die vorliegende Arbeit präsentiert neue Erkenntnisse über die quantitative Beschreibbarkeit von Strukturkonnektivität und die komplexe Beziehung zwischen struktureller und funktionaler Konnektivität in Bezug auf die Hydrologie der ungesättigten Zone. Das Hauptaugenmerk dieser Arbeit ist, in wie fern eine komplexe Struktur auf wenige aussagekräftige Konnektivitätsmaße reduziert werden kann, welche eine Vorhersage des effektiven hydraulischen Verhaltens ermöglichen. Zu diesem Zweck, werden einige gut definierte Referenzheterogenitätsmodelle mit deutlichen Unterschieden bezüglich ihrer Strukturkonnektivität eingeführt. Verschiedene Strukturkonnektivitätsmaße werden anhand ihrer Eignung verglichen morphologische Unterschiede der Referenzmodelle wiederzugeben. Der Vergleich umfasst so verschiedene Maße wie Autokovarianz, Minkowski-Funktionen, Sehnenlängenverteilung, lokale Perkolationswahrscheinlichkeit und paarweise Konnektivitätsfunktion. Mittels stochastischem Rekonstruktionsansatz wird demonstriert, dass eine kombinierte Mehrpunktstatistik bestehend aus Minkowski-Funktionen und Sehnenlängenverteilung ausreicht um Strukturkonnektivität mit geringem rechnerischen Aufwand reproduzieren zu können.

Die Referenzheterogenitätsmodelle und ihre stochastisch rekonstruierten Gegenstücke werden anschließend hinsichtlich funktionaler Konnektivität für verschiedene Prozesse und Zustände verglichen. Hierfür werden zweidimensionale, numerische Experimente zu stationärem gesättigtem Fluss, konservativem Stofftransport und hydraulischem Ungleichgewicht bei Infiltration in einen ungesättigten Boden durchgeführt. Es werden funktionale Konnektivitätsmaße

für jeden Prozess eingeführt, die stets auf dem Verhältnis zwischen effektivem hydraulischen Verhalten und einem Erwartungswert beruhen, welcher aus Eigenschaften des zu Grunde liegenden Parameterfeldes abgeleitet wird. Um dies zu erreichen, wird effektives Ungleichgewicht als ein neues Konzept eingeführt, welches die Entkopplung von gemitteltem Wassergehalt und gemitteltem Matrixpotenzial an der Infiltrationsfront aufgrund von präferenziellem Fluss beschreibt. Eine kritische Frage dabei ist, wie sich die Zustandsgrößen während transienter Bedingungen mitteln lassen. Das flussgewichtete Potenzialmittel stellt sich diesbezüglich als besonders geeignet heraus, da es hydraulisches Ungleichgewicht während des *Upscalings* konserviert. Folglich, kann effektives hydraulisches Ungleichgewicht als die Diskrepanz zwischen dynamischer und Gleichgewichtswasserretention beschreiben werden. Dies lässt sich ferner als ein Maß für Energiedissipation aufgrund von Flussbündelung in präferenziellen Fließbahnen interpretieren.

Es zeigt sich dass eine gute Reproduktion von Strukturkonnektivität auch zu einer guten Reproduktion funktionaler Konnektivitätsmaße führt. Folglich, besitzen die untersuchten Mehrpunktstatistiken tatsächlich eine gewisse Vorhersagekraft von effektiven hydraulischen Verhalten. Es stellt sich jedoch auch heraus, dass Strukturkonnektivität effektive Fluss-, Transport- und Ungleichgewichtsmerkmale in unterschiedlichem Ausmaß beeinflusst. Flusskonnektivität reagiert empfindlich auf die Kontinuität schneller Fließbahnen, wohingegen Transportkonnektivität eher auf allgemeinen Formeigenschaften des Fließfeldes beruht. Hydraulisches Ungleichgewicht hängt wiederum von einem empfindlichen Gleichgewicht aus vertikalen und lateralen Flusskomponenten ab. Somit muss funktionale Konnektivität als ein Prozess- und zustandsabhängiger Begriff aufgefasst werden.

Schlagwörter: Konnektivitätsmaße, stochastische Rekonstruktion, stationärer Fluss, Stofftransport, hydraulisches Ungleichgewicht, Upscaling

Contents

1	Introduction	1
1.1	Scope of the thesis	1
1.2	Objectives	8
1.3	Outline	9
2	Theoretical background	13
2.1	Vadose zone hydrology	13
2.2	Miller similarity	15
2.3	Averaging of state variables	17
3	Methods	23
3.1	Quantification of structural heterogeneity	23
3.1.1	Heterogeneity models with different connectivity	23
3.1.2	Structural connectivity metrics	25
3.2	Stochastic reconstruction of structural heterogeneity	33
3.2.1	Simulated annealing	33
3.2.2	Reconstruction details	35
3.3	Setup of numerical experiments	37
3.3.1	Stationary flow and transport	37
3.3.2	Infiltration	39
3.4	Functional connectivity metrics	41
3.4.1	Channeling and solute spreading	41
3.4.2	Hydraulic non-equilibrium	43
4	Results	47
4.1	Stochastic Reconstruction	47
4.1.1	Single- and Multi-objective optimization	47

4.1.2	Estimators of Structural Connectivity	50
4.2	Steady-state flow and transport	52
4.2.1	Estimators of functional connectivity	52
4.2.2	Solute breakthrough curves	54
4.3	Hydraulic non-equilibrium during infiltration	55
4.3.1	Heterogeneity effects on front propagation	55
4.3.2	Heterogeneity effects on hydraulic non-equilibrium	57
4.3.3	Heterogeneity effects front morphology	59
4.3.4	Time-dependency of hydraulic non-equilibrium	60
5	Discussion	63
5.1	Structural connectivity as a concept	63
5.2	Relation between structural and functional connectivity metrics	66
5.3	Critique on flux-weighted pressure heads	67
5.4	Impact of connectivity on hydraulic non-equilibrium	69
5.5	Relation between functional connectivity metrics	70
6	Conclusions	73
6.1	What constitutes structural connectivity?	73
6.2	What governs functional connectivity?	74
6.3	Outlook	75
A	Functional normalization	79

List of Figures

1.1	Scheme of the causal link between structural and functional connectivity.	4
2.1	Water retention curve and conductivity function of a Miller medium	16
3.1	One realization of a Multigaussian heterogeneity model (MG), a connected band heterogeneity model (CB) and macropore heterogeneity model (MP)	24
3.2	Comparison of 30 realizations of the MG and CB heterogeneity model by means of the histogram and the autocorrelation function	25
3.3	Binary images of the MG and the CB structure in Figure 3.1 thresholded at the percolation threshold of the MG structure and the CB structure	26
3.4	Comparison of Euler numbers as a function of threshold for the MG and the CB structure for 30 realizations each	28
3.5	Comparison of the two-phase two-directional chord length distribution and the mean chord length of white and black level sets for 30 realizations of the MG and CB structure	29
3.6	Comparison of local percolation probabilities as a function of window size for 30 realizations of the MG and CB structure	31
3.7	Pair connectivity function and connectivity length for the MG and CB structure	32
3.8	Evolution of energy $\log_{10}(E)$ and acceptance rate p_k for a single-objective optimization of Minkowski functions	36

3.9	Magnitude of flux density and solute concentration after infiltration of 0.5 pore volumes of solute for one realization of the MG and CB heterogeneity model depicted in Fig. 3.1.	39
3.10	Pressure head after 70 min of infiltration with $j = 2.22 \times 10^{-5} \text{ ms}^{-1}$ for the different heterogeneity models	40
3.11	Comparison of breakthrough curves for 30 realizations of the MG and CB heterogeneity model and its derivative with respect to time	41
3.12	Comparison of flow and transport connectivity indicators CF and CT for 30 realizations of the MG and CB structure	43
3.13	Evolution of averaged pressure heads at a horizontal control line at the passage of an infiltration front	44
4.1	One realization of stochastic reconstruction of a MG heterogeneity model and a CB heterogeneity model with four different structural connectivity metrics	49
4.2	Local percolation probability for 30 realizations of MG structures and the CB structures for binary images at the specific percolation threshold of the MG and CB images	50
4.3	Mean connectivity range as a function of grey value threshold for reference and reconstructed images of the MG structure	51
4.4	Comparison of flow and transport connectivity indicators CF and CT between the reference heterogeneity model and the reconstructions for the MG structure and the CB structure	52
4.5	Breakthrough curve for 30 realizations of the reference MG (left) and CB (right) structures and the mean breakthrough curve of the corresponding reconstructions	54
4.6	Evolution of mean vertical flux density at the control line for the different heterogeneity models	55
4.7	Evolution of vertical gradients in hydraulic head and water contents at the control line for the different heterogeneity models	57
4.8	Evolution of state variables at the control line for the different heterogeneity models	58
4.9	Magnitude of flux density after 70 min of infiltration with $j_0 = 2.22 \times 10^{-5} \text{ ms}^{-1}$ for the different heterogeneity models	58

4.10	Front spreading for different heterogeneity models (MG,CB,MP) expressed as the standard deviation of locations with maximum vertical head gradient plotted against mean depth of the maximum gradient	59
4.11	Comparison between hydraulic non-equilibrium and front irregularity for every realization	60
4.12	Evolution of the deviation of dynamic pressures and dynamic water contents from an equilibrium state as a function of the proportion of the control line that has already been traversed by the front	61
5.1	Level set of the reference and reconstructed CB structures thresholded at the percolation threshold of the reference structure . . .	65
5.2	Vertical profile of averaged pressure heads $\langle h_m \rangle_j$ and averaged water contents $\langle \theta \rangle$	67
5.3	Evolution of the deviation of dynamic pressures (left) and dynamic water contents (right) from an equilibrium state as a function of time for different heterogeneity models	69
5.4	Comparison of effective hydraulic non-equilibrium and effective saturated conductivity via ζ and CF and effective solute spreading via CT for the MG, CB and MP model	71
A.1	Functional renormalization of averaged water contents at a horizontal control line	80

Publications

The present doctoral thesis is partly based upon the following publication:

Schlüter, S., Vogel, H.-J., 2011. On the reconstruction of structural and functional properties in random heterogeneous media. Advances in Water Resources 34 (2), 314–325.

In particular, this includes Sections 3.1, 3.2, 4.1 and some parts of the discussion and conclusions in Chapter 5 and 6. Yet, the content has been reworked in terms of (i) a new set of hydraulic parameters that is consistent with the rest of the thesis, (ii) additional realizations for each heterogeneity model to broaden the statistical basis, (iii) extended information on methodological aspects and (iv) occasionally also new figure styles.

Chapter 1

Introduction

1.1 Scope of the thesis

Spatial heterogeneity is an ubiquitous feature of natural porous media and a source for the most interesting and complex phenomena in water and solute movement in the subsurface. During the past half-century a large body of literature has evolved that substantially improved our understanding of the effects of subsurface heterogeneity on effective flow and transport behavior. The enduring challenge and motivation is to characterize subsurface heterogeneity in such a manner, that it facilitates or improves model predictions on diverse physical processes in porous formations.

The advancements in this respect can be divided into three main phases (de Marsily et al., 2005; Renard and Allard, 2011). In the first phase, spatial heterogeneity was modeled as a mosaic of homogeneous regions typically denoted as facies, strata or horizons in their respective fields. The delineation of these homogeneous regions was typically based upon maps and field surveys and equivalent properties were estimated from averages of a limited number of measurements or from model calibration. The second phase started with the introduction of geostatistics and stochastic approaches to subsurface hydrology (Matheron, 1967; Freeze, 1975; Bakr et al., 1978; Delhomme, 1979). The small scale variability of material properties was by then considered as a key feature, that had to be represented properly in a statistical sense. The frequency distribution and the covariance of permeabilities, also denoted as second-order statistics, served as a basis to thoroughly represent the struc-

ture of heterogeneous aquifers. Simplifying assumptions like a log-normal frequency distribution of permeabilities and a Multigaussian heterogeneity model facilitated a series of analytical solutions for flow and transport problems in groundwater (Dagan, 1986, 1989; Gelhar, 1986, 1993) and the vadose zone (Yeh et al., 1985; Mantoglou and Gelhar, 1987). The appeal of the Multigaussian heterogeneity model is its parsimony, since spatial variability is fully captured by the variance of log-normal permeabilities and the correlation length, which covers the characteristic spatial scale of variability. However, the Multigaussian assumption entails some restrictions on the morphology of the underlying structure, especially the low connectivity of extreme values like barriers of low permeability and channels of high permeability, that are frequently violated by natural porous formations. The awareness of this shortcomings lead to a third phase in which the connectivity of subsurface structures came into focus (Journal and Deutsch, 1993; Gómez-Hernández and Wen, 1997). Pioneering studies demonstrated that even though heterogeneity fields share identical second-order statistics hydraulic behavior can differ vastly depending on its connectivity characteristics (Sánchez-Vila et al., 1996; Wen and Gómez-Hernández, 1998; Vogel, 2000; Zinn and Harvey, 2003). Since then new studies are continuously being published that aim at an improved statistical description of spatial connectivity by adapting methods from such diverse scientific fields as petroleum engineering, condensed matter physics or image processing and many neighboring fields like geomorphology, surface hydrology and landscape ecology. Recently, a comprehensive review on these advancements with focus on groundwater hydrology was provided by Renard and Allard (2011). This thesis adopts this line and presents some novel insights into the approaches to quantify structural connectivity and to model the effects of connectivity on functional behavior in the realm of vadose zone hydrology.

Some clarification on terms and concepts is necessary in the first place. The meaning of connectivity is intuitively clear from our everyday experiences. Yet, it lacks a rigorous mathematical definition and is rather a context-dependent concept. Most of the definitions reoccurring in literature can be grouped into two categories, static and dynamic connectivity (Renard and Allard, 2011). The first refers to the spatial distribution of parameters tacitly assuming that it does not change with time. It can then be broadly defined as the existence of

a path for flow and transport from one location to another. Two-point statistics like the autocovariance function belong to this group. The term two-point means that the probability of a certain value at one location is deduced from a known value at a second location. This turns out to be a weak connectivity metric, since the structure between the two locations is not addressed, i.e. whether there exists a connected path between the two locations or not. A corrective in this regard are provided by multi-point statistics and concepts from percolation theory that will be introduced in the course of this thesis. Some authors prefer the term statistical or structural connectivity over static connectivity to omit the temporal aspect and highlight the fact that it solely depends on the underlying structure (Knudby and Carrera, 2005; Schaap et al., 2008). The second category, dynamic connectivity, comprises metrics that characterize functional behavior with respect to a certain physical process. Typically, the upscaled functional behavior of the domain of interest is evaluated and related to some reference value derived from known properties of the underlying heterogeneous parameter field. The most intensively studied case is the effective saturated conductivity of a block with small scale heterogeneity (Wen and Gómez-Hernández, 1996; Renard and De Marsily, 1997). The ratio of this effective saturated conductivity and the geometric mean of local conductivities may serve as a flow connectivity metric that nicely reflects the degree of channeling due to preferential flow (Knudby and Carrera, 2005; Le Goc et al., 2010). Dynamic metrics for one process cannot be translated to another process. It was demonstrated that metrics of flow connectivity derived from the effective saturated conductivity and metrics of transport connectivity derived from the relation between early and mean solute arrival are in fact weakly correlated (Knudby and Carrera, 2005, 2006). On top of that, dynamic metrics depend on the state of the system and the applied boundary conditions. This is crucial for non-linear systems like the vadose zone where e.g. effective flow properties change dramatically with the degree of saturation. From here on dynamic connectivity and functional connectivity will be used as synonyms and renamed as e.g. flow or transport connectivity when the process is stressed.

A functional connectivity metric will be linked to some extent to a structural connectivity metric, depending on whether or not the structural features that govern the observed functional behavior are adequately captured. This

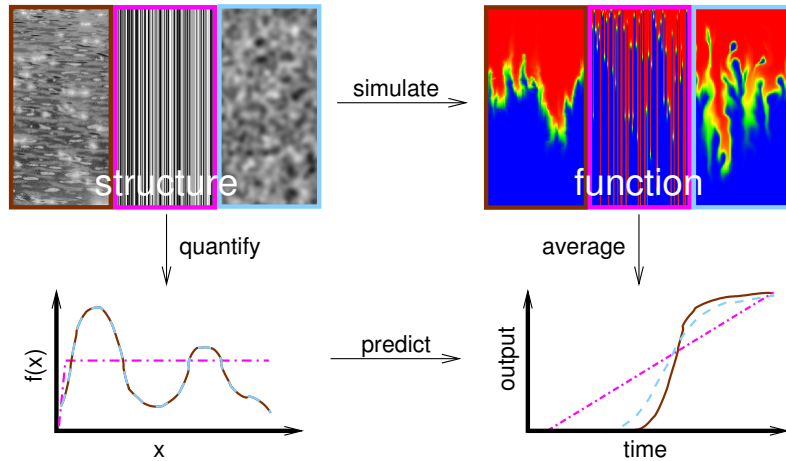


Figure 1.1: Scheme of the causal link between structural and functional connectivity.

situation is depicted schematically in Figure 1.1. One realization of three different heterogeneity models are depicted side by side. Each possesses a different internal structure at least from a visual point of view. These images shall resemble a parameter field that serves as a model domain to simulate a physical process, say solute movement. All simulations operate with identical initial conditions and boundary conditions and yet, as far as the upscaled solute transport behavior is concerned, the simulation results will be quite different which is depicted with some fictive breakthrough curves. The $f(x)$ "structure function" represents a fictive structural connectivity metric. On the one hand it can be considered as suitable metric, since it is able to distinguish between the two structures represented by the brown and magenta signatures that also exhibit vastly different solute transport properties. On the other hand, the predictive power is limited, since the effective solute transport depicted in light blue, is different, even though the structure functions $f(x)$ are identical. The opposite scenario may also occur: In spite of different $f(x)$, two parameter fields might evoke identical effective transport behavior. This raises the questions what minimum amount of morphological description is required to predict effective hydraulic behavior in heterogeneous structures. A conclusive answer is not only appealing from an academic perspective, but also practically relevant: Following the counter clockwise approach in Figure 1.1 is elegant and computationally efficient, whereas the clockwise, brute-force approach of a numerical simulation is computationally more demanding. De-

tailed information on specific transport patterns is obtained though, but this is even irrelevant when the focus is on averaged, effective behavior.

Simulating heterogeneity fields by means of stochastic reconstruction has proven to be a versatile validation tool to explore the causal link between structural heterogeneity and effective hydraulic behavior (Allard and HERESIM Group, 1993; Ouenes et al., 1994; Koltermann and Gorelick, 1996; Carle and Fogg, 1997; Deutsch and Journel, 1998; Yeong and Torquato, 1998; Talukdar et al., 2002; Strebelle, 2002; Okabe and Blunt, 2005; Čapek et al., 2009; Jiao et al., 2009; Mariethoz et al., 2010). The rationale is to measure a structural connectivity metric on a heterogeneity model of interest and to generate a new stochastic model obeying exactly this metric while other properties are random. The outcome then can be validated by (i) visual inspection, i.e. whether realizations of the original and the reconstructed heterogeneity models resemble each other, by (ii) structural connectivity metrics not included in the reconstruction or by (iii) functional connectivity metrics, i.e. comparing the functional connectivity metrics of the reference and the stochastic model to check whether some metric is really capturing structural features that steer the functional response. This strategy will be followed in this thesis, too.

In a first exercise steady-state flow and transport simulations under saturated conditions will serve as basis for functional metrics. By this, comparability with previous findings from groundwater hydrology (Zinn and Harvey, 2003; Knudby and Carrera, 2005; Le Goc et al., 2010) is possible. These studies explored the impact of structural heterogeneity on effective hydraulic conductivity and solute dispersion at single-phase flow. Zinn and Harvey (2003) started from a two-dimensional Multigaussian heterogeneity model for which the effective permeability is known to equal the geometric mean of local permeabilities and solute transport is known to display Fickian behavior. A special feature of the Multigaussian heterogeneity model is that locations with medium permeability values have highest continuity, whereas locations of low and high permeability remain isolated (Journel and Deutsch, 1993; Gómez-Hernández and Wen, 1997). Then, the authors applied a so-called absolute value transformation that altered the internal structure towards highest continuity of barriers with low permeability or highest continuity of channels with high permeability, while univariate and bivariate distributions of the permeability field remain un-

changed. Numerical simulations demonstrated that effective permeability decreases in the presence of low permeability barriers, whereas it increases in the presence of high permeability channels. Moreover, macrodispersion starts to become non-Fickian in connected structures of high permeability, i.e. it cannot be described with an effective convection-dispersion equation anymore. That is to say, the structure with isolated regions of low permeability surrounded by a well-connected pattern of high permeability evokes physical mobile-immobile domain mass transfer exhibiting faster arrival and longer tailing. These findings are in line with many field experiments in highly heterogeneous aquifers (Fogg, 1986; Poeter and Townsend, 1994; Harvey and Gorelick, 2000; LaBolle and Fogg, 2001). Knudby and Carrera (2005) elaborated on the same heterogeneity models and numerical experiments and compared various, easily obtainable indicators of effective flow and transport behavior by their ability to describe the aforementioned changes in hydraulic behavior due to different structural connectivity. That is, indicators of flow connectivity describe the flow rate increase caused by preferential flow paths, whereas indicators of transport connectivity estimate the existence of fast paths allowing early solute arrival. Moreover, they surveyed indicators of structural heterogeneity with regard to their informative value on connectivity. Remarkably, the correlation between indicators of structural connectivity and functional connectivity is low. Moreover, the dependence between flow and transport indicators is weak which is why they concluded that functional connectivity is a process dependent concept.

Since then the work has been extended to unsaturated media with the same heterogeneity models at hand (Neuweiler and Cirpka, 2005; Neuweiler and Vogel, 2007). Also, unsaturated hydraulic conductivity turns out to depend on structural connectivity. Moreover, the effective hydraulic conductivity could be satisfactorily predicted from empirical upscaling formulas based on structural connectivity metrics of the underlying parameter field (Samouëlian et al., 2007).

All numerical studies mentioned above have been based on the assumption of stationary flow. However, focusing only on steady-state properties is a restriction without a cause. In fact, Knudby and Carrera (2006) explored in another numerical groundwater study the benefit of using apparent diffusivity

as a functional connectivity metric for effective non-equilibrium behavior. In short, apparent diffusivity is an indicator of transient hydraulic behavior that describes how fast a pressure change is propagated through a domain. The authors demonstrate that the correlation between structural connectivity and apparent diffusivity is higher than the correlation between structural connectivity and indicators of stationary properties like effective permeability or early solute arrival in a stationary flow field. Moreover, the correlation between apparent diffusivity and either flow or transport connectivity is higher than the sole correlation between flow and transport connectivity. Hence, the authors concluded that apparent diffusivity accounts both (i) for structural connectivity effects controlling the average plume movement (via effective permeability) and (ii) for structural connectivity effects not linked to the effective medium properties that control the progression of the solute front.

In the course of this thesis, this approach will be extended towards unsaturated conditions. While abrupt pressure changes do rarely occur in an aquifer unless it is enforced by a pumping test, in the vadose zone these are quite frequent due to the relatively fast changing, external forcing at the atmospheric boundary. A notorious example is rapid water infiltration into a dry soil during a heavy rainstorm. Structural heterogeneity in soils is known to cause preferential flow into macropores during such an event (Beven and Germann, 1982; Roth et al., 1991; Ghodrati and Jury, 1992; Flury et al., 1994; Hendrickx and Flury, 2001; Clothier et al., 2008). Thereby, quick infiltration into macropores bypasses a large proportion of the soil, which entails hydraulic non-equilibrium at the infiltration front. This means that water content and water potential in a given control volume, are not in equilibrium according to some equilibrium water retention curve (Jarvis, 2007; Vogel et al., 2010a). That is to say, averaged state variables in a heterogeneous control volume comprising water filled macropores and a surrounding dry matrix diverge from an equilibrium retention curve and relaxes back to another equilibrium state, when the infiltration front has passed the control volume entirely. Since flow paths adapt to the structural heterogeneity of the porous medium, there is a direct link between structure and non-equilibrium. The question arises, whether structural connectivity tends to increase or decrease the degree of hydraulic non-equilibrium. To this end, new indicators of functional connectivity will be introduced that

are capable of describing hydraulic non-equilibrium and can be compared to connectivity metrics of the underlying structure.

As Figure 1.1 implies these new metrics have to be deduced from averaged state variables, i.e. the average water content and the average matric potential in a given control volume. This substitution of a heterogeneous domain of local properties by an averaged homogeneous one, with so-called equivalent or effective properties is also denoted as upscaling (Rubin, 2003; Vereecken et al., 2007). Equivalent or effective means that the functional response to some applied boundary conditions are identical for the heterogeneous domain and the upscaled homogeneous domain. Since infiltration is predominantly a vertical process averaging across a control volume with large horizontal extent is feasible whereas a high vertical resolution must be maintained (Vogel et al., 2010a). Hence the upcoming task will be to upscale a two-dimensional infiltration study into a one-dimensional effective model such that hydraulic non-equilibrium is conserved during upscaling. If successful, we can quantify the effective hydraulic non-equilibrium and relate it to other metrics of interest.

1.2 Objectives

The motivation of this thesis is that effective hydraulic behavior is not only governed by the variance and the spatial correlation of a heterogeneous parameter field, but also by the connectivity of the underlying structure. This induces the hypothesis that structural connectivity can be reduced to some meaningful metrics that facilitate the prediction of effective hydraulic behavior. Hence, the objective of this work is to test this hypothesis and to find out what structural connectivity metrics this would be.

The feature of interest in this thesis will be local zones of high hydraulic conductivity, from now on denoted as high-K zones. Accordingly, structural connectivity of a heterogeneous domain describes the existence of continuous high-K paths between distant locations. Different heterogeneity models with high and low connectivity of high-K zones will serve as reference structures at which the capability of various structural connectivity metrics to capture different degrees of connectivity can be tested. Some of them measure local properties of the structure with minimum effort and within short ranges only,

whereas others measure global properties of the entire structure at higher computational cost. Then, the aforementioned stochastic reconstruction paradigm will be applied to generate stochastic structures that exactly reproduce these short-range connectivity metrics. Subsequently, the long-range connectivity of high-K zones will be compared between the reference models and the reconstructed models.

The causal link between structural and functional connectivity will be explored by several numerical experiments. Averaging the simulation outcome yields effective hydraulic behavior with respect to different physical processes such as (i) stationary, single-phase flow, (ii) transport of a conservative tracer in a steady-state flow field and (iii) hydraulic non-equilibrium during infiltration. Functional connectivity metrics will be introduced for each process. Finally, a comparison between structural and functional connectivity metrics between different reference and reconstructed heterogeneity models provides the foundations to comment on the hypothesis.

1.3 Outline

This thesis is based on theoretical considerations and numerical simulations in the realm of vadose zone hydrology. **Chapter 2** provides the theoretical foundations in this regard. The fundamental equations for water flow and solute transport in the unsaturated zone are introduced first. Then, Miller similarity is explained, which serves as a simple and yet flexible concept to incorporate soil heterogeneity into hydraulic modeling. Finally, averaging of state variables under stationary and transient conditions is elucidated, which is a prerequisite to calculate effective hydraulic properties.

Chapter 3 provides all details on the methodology of the thesis. A comparison between three different heterogeneity models comes first together with a description of how to generate them. These will serve as reference heterogeneity models with distinct differences in structural connectivity. In the following, these structural differences are assessed by various structural connectivity metrics, all exhibiting a different ability to detect connectivity. Subsequently, simulated annealing is introduced as a global optimization method for stochastic reconstruction of the above mentioned reference heterogeneity

models. Both the general functioning and the specific parameter settings of the applied optimization method is explained. Afterwards the setup of two numerical experiments is delineated in detail. The first comprises a combination of stationary gravity flow under saturated conditions and a subsequent transport experiment of a non-sorptive tracer within that steady-state flow field. Visual differences in flow patterns due to the underlying structural heterogeneity are already discussed here. The second numerical experiment is an infiltration study in which hydraulic non-equilibrium is evoked. Here, it is demonstrated that the choice of the averaging procedure of state variables has severe implications on the effective description of hydraulic non-equilibrium. It is proposed that flux-weighted averages of matric potential result in an equivalent potential that conserves hydraulic non-equilibrium during upscaling. The chapter ends with an introduction of functional connectivity metrics, which are based on the effective flow and transport properties in the first experiment and on effective hydraulic non-equilibrium in the second experiment. The steady-state flow and transport connectivity metrics are only briefly discussed and compared, since they are already well-established. The non-equilibrium connectivity metric, however, is explained in detail, since this is a novel approach which quantifies the difference between equilibrium and non-equilibrium water retention.

Chapter 4 compiles all results that are necessary to tackle the working hypotheses stated above. First, the outcome of stochastic reconstruction of two different reference heterogeneity models are surveyed. This comprises a visual inspection whether the reference structures and the reconstructed counterparts look alike and an additional validation by structural connectivity metrics that capture long-range connectivity features. This allows for a classification on the suitability of different local connectivity metrics to reproduce structural connectivity. Secondly, functional connectivity metrics for flow and transport are compared between the reference and the reconstructed structures. This provides an answer on whether or not differences in long-range connectivity directly translate into differences in effective hydraulic behavior. Finally, the degree of effective hydraulic non-equilibrium during infiltration is compared between all three reference heterogeneity models. This is underpinned with additional hydrological and morphological properties of the infiltration front.

Chapter 5 includes a comprehensive discussion on the results. First, the impact of short-range, structural properties on structural and functional connectivity is analyzed by a detailed inspection of structural artifacts from stochastic reconstruction. Then, the results of the infiltration study are discussed from different perspectives: (i) a final critique on a novel approach to quantify hydraulic non-equilibrium is made by comparing it to observations from field and lab experiments, (ii) the impact of structural connectivity on effective hydraulic non-equilibrium is interpreted and (iii) the relation between functional connectivity metrics for flow, transport and hydraulic non-equilibrium is assessed.

Finally, **Chapter 6** reconsiders the working hypothesis that have been stated in the beginning. In the first place, it provides a final statement on which structural properties contain sufficient information on connectivity to predict flow, transport and hydraulic non-equilibrium. Furthermore, the relationship between effective hydraulic behavior is finally being judged. The thesis ends with an outlook on future perspectives of the developed methods.

Chapter 2

Theoretical background

2.1 Vadose zone hydrology

A porous medium is composed of solid matter and the pore space in between. In unsaturated soils this pore space is partly filled by air and water. The ratio of water volume to total volume defines the water content θ , which depends on the prevailing matric potential ψ . This matric potential expresses energy density of water due to capillary forces. It is defined as the amount of work per unit quantity of pure water that is required to remove an infinitesimal quantity of water (Hillel, 1998). Matric potential ψ_m and gravitational potential ψ_z constitute total hydraulic potential ψ . Hydraulic potential is an energy density [J m^{-3}] which is equivalent to pressure [Pa]. This pressure is frequently expressed in terms of an equivalent height of a water column [m] and then denoted as hydraulic head. Head units are more convenient for some equations, which is why they will be used in this study. A unique and highly non-linear relationship between water content θ and pressure head h_m exists that is denoted as water retention curve or soil water characteristic $\theta(h_m)$. However, this uniqueness is only fulfilled, if (i) the solid matter is rigid, (ii) the soil water is stagnant and (iii) hysteresis is neglected. Different models exist that describe $\theta(h_m)$ by empirical parameterizations, of which the van Genuchten model (van Genuchten, 1980) is most frequently used:

$$\Theta(h) = \{1 + [\alpha|h_m|]^n\}^{-1+1/n} \quad (2.1)$$

where $\Theta = (\theta - \theta_r)/(\theta - \theta_s)$ is water saturation, θ_s and θ_r are saturated and residual water content and α and n are shape parameters, referring to the air-entry point and steepness in saturation decline, respectively. Under saturated conditions all pores are water-filled and a unique value of hydraulic conductivity K_s exists that solely depends on pore architecture. In unsaturated soil, however, hydraulic conductivity is a non-linear function of water saturation and varies by orders of magnitude as flow is restricted to the water-filled pores. Again, various expressions exist to describe unsaturated conductivity K as a function of Θ . Most common is the Mualem formulation (Mualem, 1976) in combination with eq. 2.1:

$$K(\Theta) = K_s \Theta^\tau \left\{ 1 - \left[1 - \Theta^{n/(n-1)} \right]^{1-1/n} \right\}^2 \quad (2.2)$$

where K_s is saturated conductivity and τ is a tortuosity parameter that controls the decline in $K(\Theta)$. According to Darcy's Law K is a proportionality factor with unit of a velocity [ms^{-1}] that relates gradients in hydraulic head, as the driving force, with the resulting flux that it evokes. Combining this fundamental relationship with the conservation of mass results in Richards equation, which is the standard equation for dynamics of water flow in soil. Formulated in terms of hydraulic head it reads

$$C(h_m; \mathbf{x}) \partial_t h_m - \nabla \cdot [K(h_m; \mathbf{x}) [\nabla h_m + z]] = 0, \quad (2.3)$$

where $C(h_m; \mathbf{x})$ is the local water capacity at location \mathbf{x} defined as the derivative of the water retention curve $C(h_m) = \partial\theta/\partial h_m$, $K(h_m; \mathbf{x})$ is the local unsaturated conductivity and z is elevation. The highly non-linear functions $C(h_m; \mathbf{x})$ and $K(h_m; \mathbf{x})$ are parameterized in the Mualem- van Genuchten formulation as described above. This equation is only valid if (i) the air-filled pore space is continuous and (ii) h_m and θ are in local equilibrium at some point on the water retention curve.

In terms of solute transport two different mechanisms of solute displacement need to be considered. One component is the convective transport proportional to the water flux, the other is the dispersive displacement including hydrodynamic dispersion as written below. Adding up both and imposing mass conservation results in the convection-dispersion equation

$$\theta \partial_t C_w + j \nabla C_w - \nabla [D_{\text{eff}} \nabla C_w] = 0 \quad (2.4)$$

where C_w is the solute concentration in water, j is water flux and D_{eff} is effective dispersion comprising molecular diffusion and hydromechanic dispersion. Sorption is not considered in this formulation.

2.2 Miller similarity

In groundwater hydrology spatial heterogeneity of the aquifer manifests itself in local variations of saturated hydraulic conductivity. However, vadose zone hydrology has to cope with highly non-linear relations between saturation, water potential and unsaturated hydraulic conductivity. A Miller similar medium provides a simple and yet flexible heterogeneity model to this end (Roth, 1995; Nielsen et al., 1998; Vereecken et al., 2007) and has been used for various purposes in vadose zone modeling (Roth and Hammel, 1996; Samouëlian et al., 2007; Vogel et al., 2010a). The original intention of Miller similitude was to provide a simple model for hysteresis in homogeneous, isotropic media by linear scaling relations, in order to accommodate observations that the hydraulic behavior of an unsaturated medium depends on the water dynamics (Miller and Miller, 1956). Yet, this hysteresis model can also be restated as a model for spatial heterogeneity in that the scaling factor is considered to be a random function in space (Roth, 1995). Miller similarity refers to similarity of pore morphology and states that the porosity is constant everywhere and the local pore size distribution is shifted from a characteristic mean pore size r^* towards smaller or larger mean pore radii r by a scaling factor $\chi = r/r^*$ (Miller and Miller, 1956). Hence, this extended heterogeneity model consists of a single scaling factor varying in space and two reference functions, the soil water characteristic $h_m^*(\theta)$ and the unsaturated conductivity function $K^*(\theta)$. The constitutive scaling relations are $h_m(\theta) = \chi^{-1} h_m^*(\theta)$ and $K(\theta) = \chi^2 K^*(\theta)$. This is in line with $h_m \propto 1/r$ in the Young-Laplace equation and $K \propto r^2$ according to Pouseuilles' law. Assuming a log-normal pore size distribution in soil, $\log(\chi)$ is normally distributed with an expectation $\langle \log(\chi) \rangle = 0$ and a given standard deviation σ_χ . Setting the standard deviation of $\log(\chi)$ to $\sigma_\chi = 0.75$ and the hydraulic parameters to $\theta_s = 0.32$, $\theta_s = 0.03$, $\alpha = 0.023 \text{ cm}^{-1}$, $n = 4.2$,

$K_s = 2.22 \times 10^{-5} \text{ms}^{-1}$ and $\tau = 0.5$ leads to the hydraulic functions depicted in Figure 2.1.

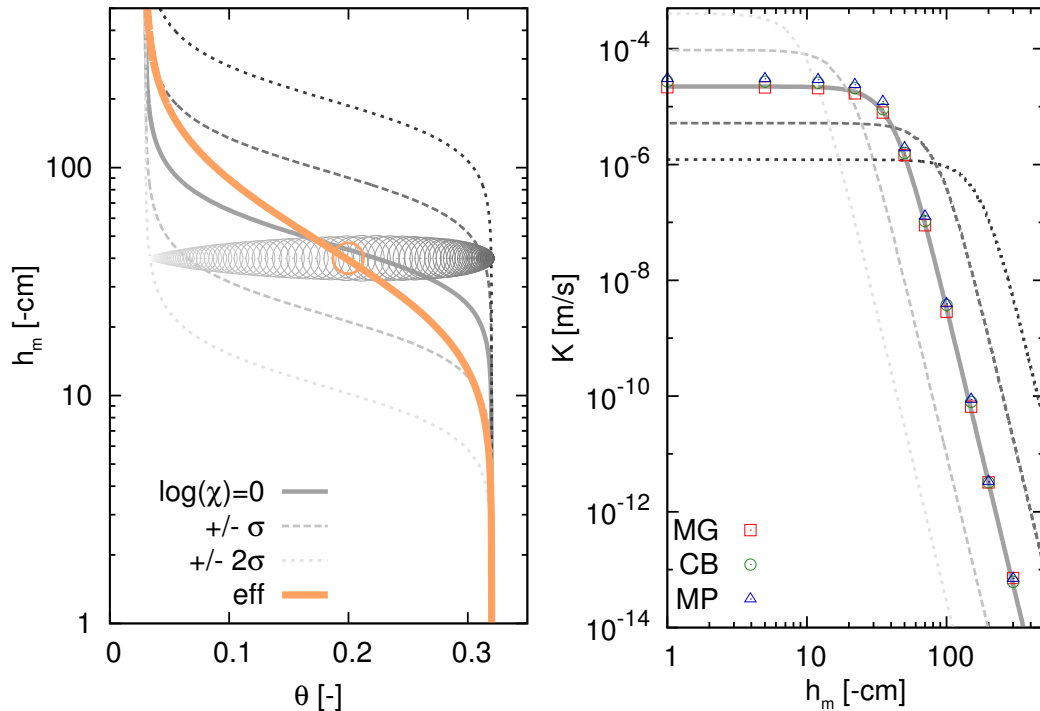


Figure 2.1: Water retention curve (left) and conductivity function (right) for the reference parametrization of a Miller medium ($\log(\chi) = 0$) and with a scaling factor of $\pm\{1, 2\}\sigma_\chi$. Left: circles of different size represent the shift in local $\theta(\chi)$ at a pressure head of $h_m = -40$ cm. The color code represents $\log(\chi)$, whereas the size represents the frequency ω_{χ_i} . Right: symbols represent $\langle K(h_m) \rangle$ at different potentials for the three heterogeneity models.

The scaling factor affects $h_m(\theta)$ by shifting the air-entry pressure (indicated by α) while the logarithmic steepness of the curve (n) is preserved, as the width of the log-normal pore size distribution remains unchanged. The impact of the scaling factors on $K(h_m)$ is twofold: a shift in air-entry pressure and in saturated conductivity, implying e.g. that a coarser material has a higher K_s but reaches its air-entry point at higher pressure heads. The other symbols in Figure 2.1 are explained in the next section, when averaging of state variables is considered.

More elaborate similarity concepts exist, which relax some conditions of Miller and Miller (1956) towards variable porosity or independent scaling factors for $\theta(h_m)$ and $K(\theta)$ for a better representation of field observations (Warwick et al., 1977; Vogel et al., 1991; Nielsen et al., 1998; Vereecken et al., 2007).

However, since the focus of this study is on theoretical foundations of spatial heterogeneity model simplicity is considered more beneficial.

2.3 Averaging of state variables

Up to this point Miller similarity has been introduced as a theoretical concept to express local variability in the hydraulic functions $\theta(h_m)$ and $K(\theta)$ by a single scaling factor χ . Moreover, different models of spatial heterogeneity will be presented that all treat χ as a random function in space but differ qualitatively in the spatial connectivity of χ . Numerical experiments will demonstrate the impact of spatial connectivity on effective hydraulic behavior. As Figure 1.1 indicates, the interest typically lies in the impact of small-scale heterogeneity on the averaged hydraulic behavior at a larger scale and far less on specific flow and transport patterns. To give a practical example: it is much more important to know how fast or whether at all a surface-applied contaminant leaches into groundwater after a heavy rain event than to know the specific location of the first arrival. Therefore, this section demonstrates how state variables θ, h_m, j, C_w and the material properties α, n and K can be represented at a larger scale. The procedure to average detailed spatial information on state variables in a domain into representative values at a coarser representation of the same domain is also denoted as upscaling (Vereecken et al., 2007). In the following, the label $\langle \cdot \rangle$ will indicate an upscaled, effective state variable obtained from direct averaging and the subscript $_{\text{eff}}$ will indicate an upscaled material property obtained from fitting. As flow and transport in the vadose zone are predominantly oriented in the vertical direction, the focus here is to calculate averaged state variables along horizontal transects perpendicular to the principal flow direction.

Since water volume is an additive property, the averaged water content within a control volume (or area or line) is easily obtained as the arithmetic mean of all local θ values, i.e. all pixels values in a digitized θ image. Considering the entire Miller medium as a control volume (or area) where the frequency distribution of scaling factors is known, the mean water content at a given pressure equals the area-weighted average of all scaled water contents (Samouëlian et al., 2007; Vogel et al., 2010a):

$$\langle \theta(h_m) \rangle = \sum_i \omega_i \theta(h_m, \chi_i) \quad (2.5)$$

where i identifies all scaling factors χ_i occurring in the domain, $\theta(h_m, \chi_i)$ is the scaled water content, ω_i is the probability density of the scaling factor χ_i with $\sum_i \omega_i = 1$. Figure 2.1 depicts an example of how $\langle \theta(h_m) \rangle$ is calculated at $h_m = -40$ cm. The grey circles depict $\theta(h_m, \chi_i)$ with different grey tones depending on χ_i and different size depending on ω_{χ_i} . Calculating $\langle \theta(h_m) \rangle$ at various pressure heads renders the equilibrium water retention curve of the medium under static conditions depicted in orange. Hence, heterogeneity merely needs to be addressed in terms of frequency distribution of scaling factors irrespective its spatial arrangement. As indicated in Fig. 2.1, the variability in $\log(\chi)$ results in a broadened pore spectrum. As a consequence, the effective hydraulic parameters of the entire soil changes from $n=4.2$ for the reference parametrization to $n_{\text{eff}}=2.30$ and $\alpha = 0.023 \text{ cm}^{-1}$ to $\alpha_{\text{eff}} = 0.031 \text{ cm}^{-1}$ for the chosen set of hydraulic parameters, whereas θ_s^{eff} and θ_f^{eff} remain unaffected. Averaging of solute concentrations in water C_w is also straightforward, since it is a capacitive property, too. Hence, the effective concentration $\langle C_w \rangle$ in a given domain equals the arithmetic mean of local C_w -values within that domain. In principle, averaged water fluxes j within a control volume could also be calculated as an arithmetic mean of local j -values. However, flux is not a scalar but a vector with different directional components. The problem is relaxed by the aforementioned fact, that the interest lies only in the vertical fluxes j_z across a horizontal transect, for which the arithmetic mean again applies.

On the contrary, the effective $K(h_m)_{\text{eff}}$ is more difficult to determine, as it is an emergent property of the entire domain and depends on the spatial arrangement of scaling factors. Therefore, we simulate gravity flow at different pressure heads, calculate $K(h_m)_{\text{eff}}$ directly from steady-state flux rates $\langle j_z \rangle$ and set h_m to the imposed boundary condition, disregarding the weak internal variability in the pressure field. The acronyms MG, CB and MP in Figure 2.1 represent different heterogeneity models as discussed below. The difference in $K(h_m)_{\text{eff}}$ between them demonstrates the impact of spatial arrangement on effective conductivity. The higher connectivity in the CB and MP heterogeneity as compared to MG heterogeneity leads to an increase in effective K_s^{eff} , which

is in line with former studies (Zinn and Harvey, 2003; Knudby and Carrera, 2005; Le Goc et al., 2010). The unsaturated conductivity is also higher in the wet range, whereas the order changes under dry conditions. As Eq. 2.1 and 2.2 do not allow for different n_{eff} , the effective $K(h_m)_{\text{eff}}$ values are fitted by a spline function .

An assumption underlying Richards equation is that water potential and water content are always in equilibrium locally with a well defined conductivity at a given saturation. The required constitutive relations are given by the water retention curve $\theta(h_m)$ and the hydraulic conductivity function $K(\theta)$. Due to the heterogeneous distribution of material properties, every location has its own specific water characteristic and conductivity function. The challenge is to determine an effective potential within a heterogeneous control volume during transient flux.

Since hydraulic head h is the sum of pressure head h_m and gravitational head h_z and flow in the vadose zone is predominantly orientated in vertical direction, the control volume typically reduces to a horizontal plane with constant gravitational head h_z and variable pressure heads h_m . Thus, in two-dimensional space the task reduces to determine the average pressure head $\langle h_m \rangle$ at a horizontal control line. If water is in hydrostatic equilibrium, h_m is constant within a horizontal plane and we can apply the averaging rules for θ and K as explained above to arrive at a complete description of hydraulic properties. This operation is also valid for steady-state equilibrium under gravity flow, provided local variations in potential are negligible (de Rooij, 2011). However, during transient conditions averaging across heterogeneous control volumes becomes a difficult task, because averaging of water potential is not clear but is still a matter of debate (Korteland et al., 2009; de Rooij, 2011). So far, no averaging approach is available that has been proven to be valid under transient conditions, particularly when gradients in hydraulic head are steep. Yet, hydraulic gradients are the driving force of water flow and need to be adequately represented in simplified upscaled models. In the following we compare four different averaging techniques for pressure head and we discuss their suitability to represent hydraulic non-equilibrium in an effective one-dimensional model:

arithmetic mean In the lack of any other physical justification one could adapt to the averaging rule already applied to water contents and calculate the arithmetic mean of local pressure heads:

$$\langle h_m \rangle_a = \frac{1}{L} \int_L h_m dL \equiv \frac{1}{n} \sum_i^n h_{m,i} \quad (2.6)$$

written as an integral for a continuous domain and as a summation for a discretized domain, respectively, where i is the location identifier and n is the amount of all pixels along the control line with width L . Note that in continuous space the control line has no vertical extent, whereas in discretized space the extent equals the size of a pixel. It has been previously applied by Zehe et al. (2006) and is also denoted as volume averaging (de Rooij, 2011). This approach is questionable, since the physical meaning of an arithmetic average with respect to the driving force at the larger scale is not clear.

θ -weighted mean It has been suggested that the involved volume of water has to be considered for averaging in order to conserve potential energy during upscaling (Whitaker, 1986; Gray, 2002; de Rooij, 2011). Thus, an intrinsic phase average was defined:

$$\langle h_m \rangle_\theta = \frac{\int_L \theta h_m dL}{\int_L \theta dL} \equiv \frac{\sum_i^n \theta_i h_{m,i}}{\sum_i^n \theta_i} \quad (2.7)$$

Herewith, the local pressure heads are weighted by the local water content. However, pressure head refers to the energy required to remove an infinitesimal small volume of water at a given state. Thus, this energy density cannot be attributed to the total volume of water and hence, the θ -weighted mean might not be an appropriated choice.

maximum An averaged value of pressure head is intended to be used as the driving force for water flow in a Richards-type model at the larger scale. Recently (Vogel et al., 2010a) proposed to use the maximum pressure head within a planar control volume

$$\langle h_m \rangle_{max} = \|h_m\|_\infty \equiv \max\{h_{m,1}, \dots, h_{m,n}\} \quad (2.8)$$

because this determines the minimum energy required to extract water from that volume.

flux-weighted mean We might assume that the water volume flowing across a horizontal plane within a heterogeneous medium is proportional to the drop in some averaged head across this plane. A way to represent this average head is to consider the flux-weighted mean potential:

$$\langle h_m \rangle_j = \frac{\int_L j_z h_m dL}{\int_L j_z dL} \equiv \frac{\sum_i^n j_{z,i} h_{m,i}}{\sum_i^n j_{z,i}} \quad (2.9)$$

where $j_{z,i}$ is the vertical flux density at the sub-compartments i . Hence, the flux weighted potential (short for flux density weighted potential) integrates spatial variations in local water potential and spatial variations in local water fluxes. As a result, only those locations where the irregular front has already passed the control line do contribute to the upscaled average pressure head.

In the remainder of the thesis, these four averaging methods for pressure head will be compared by their impact on upscaled hydraulic behavior during hydraulic-non-equilibrium.

Chapter 3

Methods

3.1 Quantification of structural heterogeneity

3.1.1 Heterogeneity models with different connectivity

Analytic solutions for effective hydraulic properties under saturated (Dagan, 1986; Gelhar, 1986) and unsaturated conditions (Yeh et al., 1985; Mantoglou and Gelhar, 1987) typically assume a Multigaussian heterogeneity model. This implies not only a normal frequency distribution function of parameter values (i.e. log-values of hydraulic conductivity), but also that the correlation structure of these values is the same above and below the mean value. That is to say, spatial statistics like the indicator variogram at given grey thresholds are identical for a field and its inverse. As a consequence, extreme values are always situated on isolated spots, whereas values around the mean have the highest continuity (Journel and Deutsch, 1993; Gómez-Hernández and Wen, 1997). This is, however, quite a restrictive assumption and frequently disproved by nature. A prominent example are macropore networks generated by biological activity with high conductivities assembled along elongated channels that are much longer than the correlation length of matrix heterogeneity (Shipitalo and Butt, 1999; Jarvis, 2007; Zehe et al., 2010). To demonstrate the impact of connectivity features we set up three different types of heterogeneity fields that are almost identical in terms of two-point statistics but different in topology (Fig. 3.1).

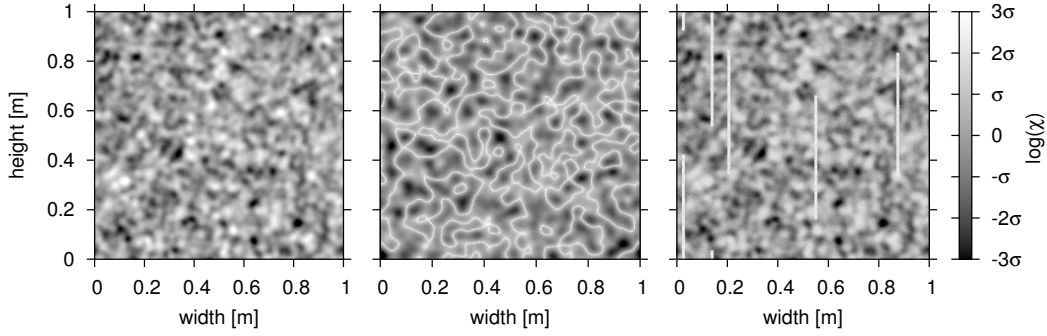


Figure 3.1: One realization of a Multigaussian random field (MG, left), a reconfigured field with high values assembled along connected bands (CB, middle) and field with Multigaussian background heterogeneity superposed by vertically oriented macropores (MP, right).

The grey values g represent the logarithm of scaling factors $\log(\chi)$ in a Miller-similar medium. The first field corresponds to the classical Multigaussian (MG) model with a Gaussian autocovariance function and a correlation length of 0.025 the image length. It is generated by means of a Fourier transform of the autocovariance function (Robin et al., 1993). In the second model the entire image is reconfigured according to the method of Vogel (2002) also used by Zinn and Harvey (2003). In short, by taking the absolute difference of any pixel to the mean and inverting the result, extreme values are assembled into connected bands (CB) of high continuity. As this operation changes the correlation length, a new MG with the altered correlation length has to be created. In the third model only a small proportion of the MG image is modified by inserting 5 vertical channels of extreme values at random locations, with a size of 0.012×0.5 the image length and assuming vertical periodicity. This geometry shall mimic the distinct anisotropy of macropores (MP) in soil. The CB and MP model differ not only in that the CB model is perfectly isotropic, it also exhibits much higher local bonding of high-K zones in comparison to the rather isolated channels in the MP model. By matching the histogram of the CB and MP model with that of the MG model (normal score transform), all heterogeneity models share the same normal frequency distribution of gray values. The same heterogeneity models have already successfully been applied in the past to determine the impact of structural connectivity on water flow and solute transport under saturated, stationary conditions (Knudby and Carrera, 2005; Le Goc et al., 2010).

3.1.2 Structural connectivity metrics

Two-Point Statistics

The histogram and the autocovariogram are fundamental one- and two-point statistics to describe the variability of a property itself and the variability in space. These distributions are depicted in Figure 3.2 for a comparison between the MG and the CB heterogeneity model. For now, the MP heterogeneity model is ignored, since it won't be examined by stochastic reconstruction in the next sections. The frequency distribution of grey values g on the left hand side is identical for all realizations of both models, as this has been enforced by the generation process. Dividing the autocovariance by the variance yields the autocorrelation function on the right hand side. The two models differ slightly. The autocorrelation at small distances is smaller for the CB model since the bands are rather thin and exhibit steep gradients towards the surrounding matrix, whereas long-range correlation is slightly higher due to the continuity of the bands. The integral of the autocorrelation function is denoted as correlation length or integral scale. This correlation length is always the same for each pair of a CB and a MG realization. As Figure 3.2 shows, there is however some inevitable variability in the long-range correlation among many realizations.

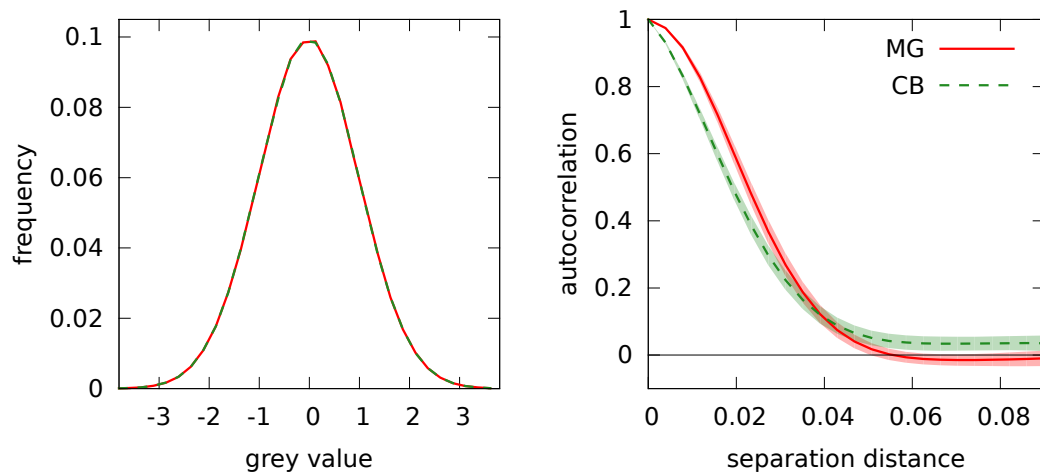


Figure 3.2: Comparison of 30 realizations of the MG and CB heterogeneity model by means of the histogram (left) and the autocorrelation function (right). Shaded area represents standard deviation. Separation distance is scaled by the image size. Grey value is normalized by $(g - \langle g \rangle) \sigma_g^{-1}$.

Evidently, the correlation length is not sensitive to connectivity features, since the autocorrelation only covers information at two distant points, without addressing the space in between. The extension from two-point to multiple-point statistics is an obvious step to improve the characterization of structural properties including connectivity. This was already proposed some decades ago (Journel and Alabert, 1989; Allard and HERESIM Group, 1993). In the following we introduce some well-established multiple-point statistics all measuring hydraulically relevant features by different means. Since these methods are based on binary domains we take advantage of the level set approach (Vogel, 2002; Samouëlian et al., 2007; Renard and Allard, 2011). Thereby, the grey scale image is successively segmented by increasing threshold values resulting in a stack of indicator maps (i.e. binary images) that are evaluated separately.

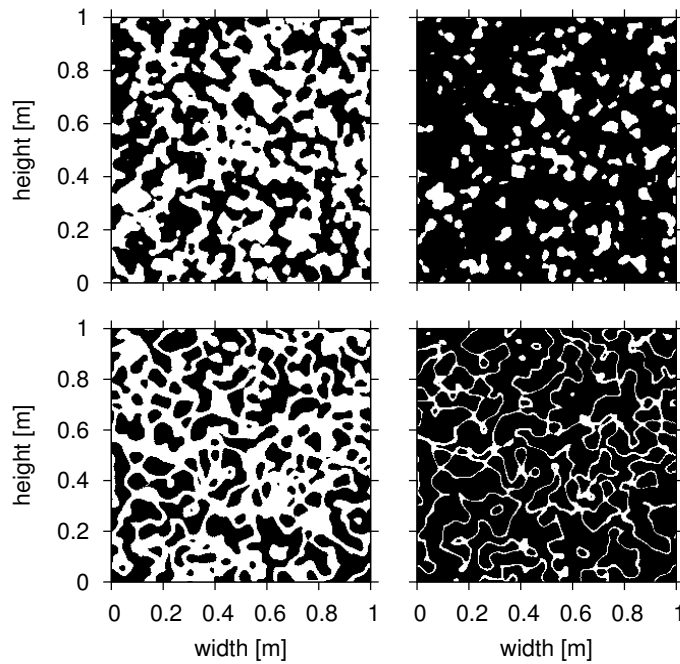


Figure 3.3: Binary images of the MG (top) and the CB structure (bottom) in Figure 3.1 thresholded at the percolation threshold of the MG structure (left) and the CB structure (right). White (black) areas represent grey values higher or equal (lower) than the threshold.

Figure 3.3 depicts two level sets each for the realization of a MG and CB heterogeneity model depicted in Figure 3.1. The grey thresholds g_t are chosen such that the set of white pixels is exactly at the percolation threshold in the MG image (left) and the CB image (right), respectively. A structure is said to percolate if a continuous path between two opposite borders exists in the

foreground phase (white). The percolation threshold of the CB image is at a higher grey threshold due to the continuity of bright bands.

Minkowski functions

It is appealing to quantify complex structures by a limited set of morphological descriptors. Minkowski functionals M_k provide a formidable means to this end (Mecke, 2000). For two-dimensional structures they include covered area (M_0), boundary length between background and foreground (i.e. black and white) (M_1), and the Euler number as a topological measure describing connectivity (M_2). The Euler number counts the number of isolated objects minus the number of redundant connections. Thus it takes negative values for well connected structures and positive values for patterns in which the objects stay rather isolated. Minkowski functionals are additive. When cutting a binary domain into parts, the sum of the partial contributions still equals the global value with respect to M_k . The elementary cell for which this additive statement still holds is a 2x2 cell. Consequently, the Minkowski functionals can be calculated very efficiently from the frequency distribution of local pixel configurations in terms of the possible values $[0, 1]$. Precisely, the frequency of 16 possible configurations within a 2x2 pixel neighborhood are counted by a single loop throughout the entire image, which reduces the Minkowski functionals to a compact four-point statistic. The different functionals are directly inferred from this frequency distribution of local configurations by attributing specific weights to each configuration. For implementation details the reader is referred to Ohser and Mücklich (2000), Mantz et al. (2008) or Vogel et al. (2010b). Taking into account the aforementioned level set approach each Minkowski functional can be expressed as a function of threshold value g_t applied to the grey scale image. The resulting functions $M_k(g_t)$ are termed Minkowski functions (Vogel et al., 2002; Samouëlian et al., 2007; Vogel et al., 2010b). Figure 3.4 depicts the Euler number as a function of threshold value for the two reference images. It has been shown by Mecke and Wagner (1991) that the zero crossing of the Euler number corresponds approximately to the percolation threshold, where a continuous path connecting the boundaries of the image can be found.

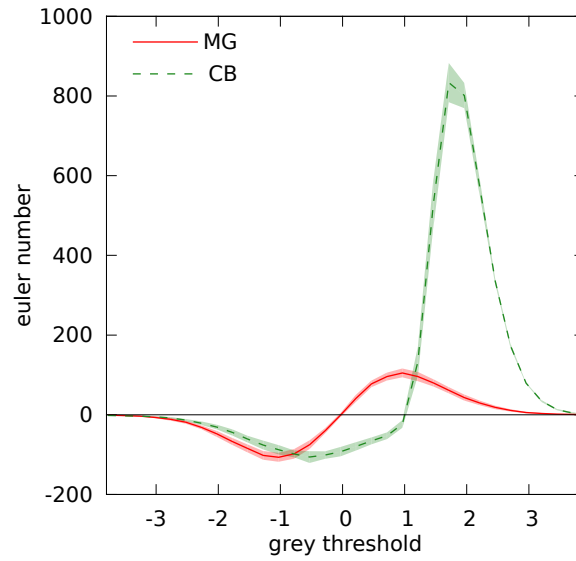


Figure 3.4: Comparison of Euler numbers as a function of threshold for the MG and the CB structure for 30 realizations each. Shaded area represents standard deviation. Grey threshold is normalized by $(g_t - \langle g \rangle) \sigma_g^{-1}$.

The sigmoidal shape, together with the zero crossing exactly at the mean grey value is typical for classical Multigaussian images. The CB image however is characterized by a shifted zero crossing towards higher grey values, which reflects the better connectedness of the bands in the range between $\mu - \sigma$ and $\mu + \sigma$ leading to more loops within the network and less isolated objects. The high positive peak at brighter grey values indicates that the thin bands are cut abruptly into a multitude of small isolated pieces. In the following we will focus on the Euler number as a topological connectivity metric. It should be noted, however, that the four-point statistic also includes area density and the boundary length density as additional morphological metrics that describe the regularity of a structure.

Chord length distribution

Chord length is defined as the distance between two intersections of a line with the two-phase boundary (Roberts and Torquato, 1999). Thus, the chord length distribution summarizes the ensemble of all linear chords occurring in an image. This is in contrast to ordinary two-point statistics, where only the endpoints of an imaginary line are considered. The chord length distribution

is phase specific, in that the distributions for both phases are independent. The chord length distribution (or the closely related lineal path function) has been successfully used for stochastic reconstruction in various former studies as a suitable tool to assess clustering within complex structures (Roberts and Torquato, 1999; Manwart et al., 2000; Talukdar et al., 2002; Čapek et al., 2009). Since connectedness is evaluated along lineal test lines it only possesses limited information on connectivity. In Figure 3.5 the chord length distributions of both phases along the principal axes are compared for the two reference images. Thereby, the grey threshold g_t was chosen to be at the zero crossing of the Euler number for the CB image.

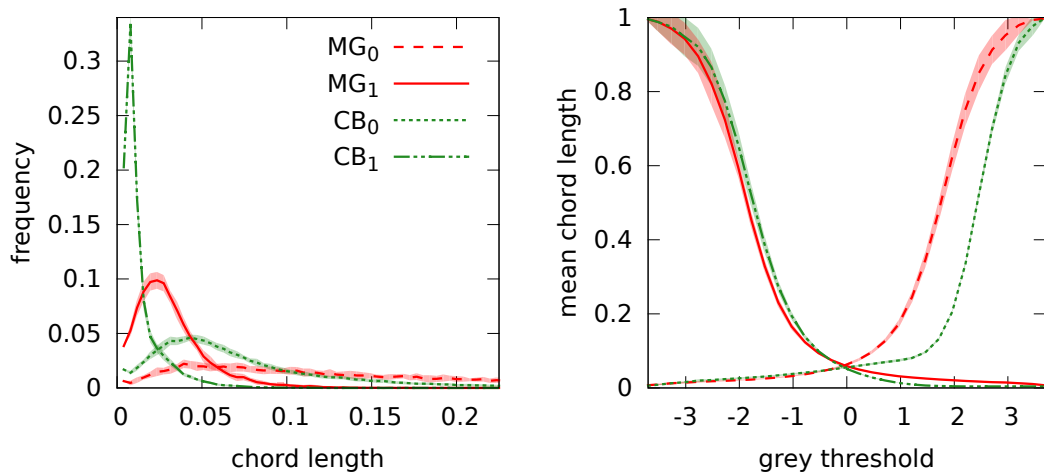


Figure 3.5: Left: Comparison of the two-phase two-directional chord length distribution for 30 realizations of the MG and CB structure thresholded at the zero-crossing of Euler numbers of CB structure (1 - white phase, 0 - black phase). Shaded areas represent standard deviation. Chord length is scaled by the image size. Right: Mean chord length of white and black level sets as a function of grey threshold. Grey threshold is normalized by $(g_t - \langle g \rangle) \sigma_g^{-1}$.

The CB image differs from the MG image in that the white phase has a pronounced peak at small chords while long chords are less frequent. This is because the bands are rather thin and very curvilinear. Also within the black phase the chord lengths are systematically shifted towards lower chord lengths due to fragmentation by the elongated bands. Evidently, the chord length distribution nicely reflects the size distribution of structural features as visually observed in Fig. 3.3. Similar to the correlation length a mean chord length (chord length integral scale) can be calculated by integrating the frequency over all lengths. Following again the level set approach Figure 3.5 compares

these mean chord lengths as a function of grey threshold for both reference structures. The striking difference between the CB and the MG structure is the mean chord length of the background (black phase) which is significantly shorter for the CB image compared to the MG image in the range from μ to $\mu + 2.5\sigma$. In contrast, the mean chord lengths for the foreground is very similar for both images. This reflects the insensitivity of the foreground chord lengths with respect to connectivity. Antoine et al. (2009) came to similar conclusions.

Local percolation probability

A structure is deemed to percolate, if a continuous path between two opposing sides (or locations) exists. Percolation theory is the most direct approach to quantify connectivity and has proven to be a powerful tool especially when disorder in the structure is high (Hunt, 2001). In contrast to the other aforementioned multi-point statistics, percolation is a global feature that can not be captured by local evaluation. Hilfer (2002) proposed the concept of local percolation probability to evaluate percolation properties of heterogeneous binary structures as a function of the size of subsamples. If L is the side length of a squared subset of a 2D image, then $p_\beta(L)$ denotes the probability that the phase $\beta = \{0, 1\}$ exhibits a continuous percolating path within the subset. It is obtained by evaluating all possible subsets of size L . The local percolation probabilities for the two reference images are compared in Figure 3.6.

The threshold g_t chosen to generate the underlying binary images corresponds to the zero crossing of Euler numbers within the MG images, indicating that the image contains just as much redundant loops within clusters as there are separate clusters within the image. This zero crossing is a formidable estimate for the percolation threshold, which means that at higher thresholds the set of brighter pixels would not percolate anymore. The mean percolation probability of 0.5 found for MG images irrespective the window size demonstrates that the structure is right at the percolation threshold. In contrast, all CB images percolate at this threshold once the subsample covers a representative area.

Since global percolation is a binomial feature the corresponding standard deviation converges to $\sigma = \sqrt{p(1-p)}$ at the right end of Figure 3.6. At small window sizes the local percolation probability approaches the porosity of the

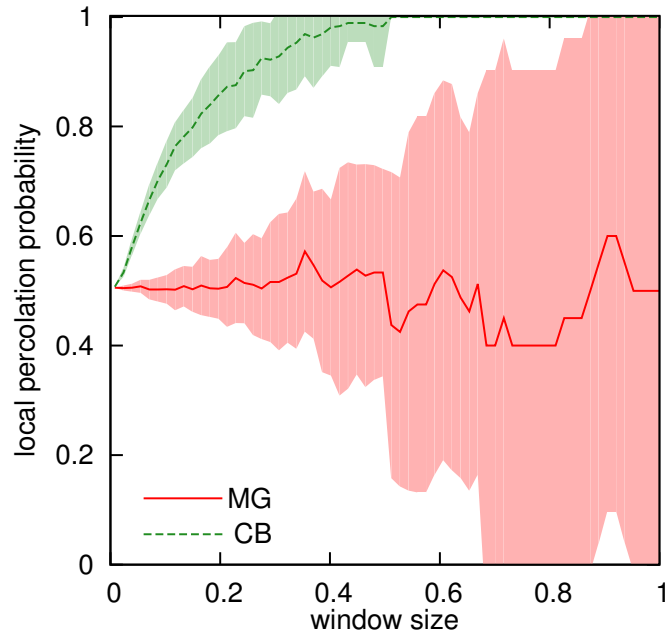


Figure 3.6: Comparison of local percolation probabilities (mean and standard deviation) as a function of window size for 30 realizations of the MG and CB structure thresholded at the percolation threshold of the MG structure. Window size is scaled by the image size.

underlying indicator map, which is identical for both structures and all realizations. The rather quick divergence into states of critical percolation and perfect percolation for the MG and the CB structure, respectively, indicates the potential of this measure to quantify connectivity. In former studies, local percolation probability turned out to be an excellent validation tool for structural connectivity (Manwart et al., 2000; Talukdar et al., 2002; Okabe and Blunt, 2005; Čapek et al., 2009). However, it is difficult to use it for stochastic reconstruction, since percolation by definition is a global feature, and thus, can not be evaluated on a local basis. This, however, is critical to maintain time efficiency during the reconstruction process.

Pair connectivity function

It has been demonstrated above that the mean chord length can hardly be interpreted towards connectivity. This is because it only considers, if there is a straight connection between two locations x and $(x+h)$. Thus, the undulating pathways of the CB images cannot be captured. To better assess connectivity it appears more adequate to consider the probability that x and $(x+h)$ are

linked by a continuous path of neighboring pixels (denoted with $x \leftrightarrow x + h$) within the subset of all pixels belonging to phase β in the domain Ω . This corresponds to the pair connectivity function $\tau(h)$ as defined by Allard and HERESIM Group (1993):

$$\tau(h) = \{x \leftrightarrow x + h \mid x \in \beta, x + h \in \Omega\} \quad (3.1)$$

This connectivity statistics combines the continuous path concept from percolation theory with the well-established lag-dependence as it is used e.g. in the autocovariance function. It has also been successfully applied as a validation tool for structural connectivity in former studies (Western et al., 2001; Knudby and Carrera, 2005; Antoine et al., 2009). For implementation details the reader is referred to Western et al. (2001). Note that the pair connectivity function is in close accordance to the two-point cluster function that had been previously defined by Torquato et al. (1988). Figure 3.7 depicts the pair connectivity function for the two reference structures. The images were binarized at the percolation threshold of the CB structures, so that the results remain comparable to the chord length distributions in Figure 3.5.

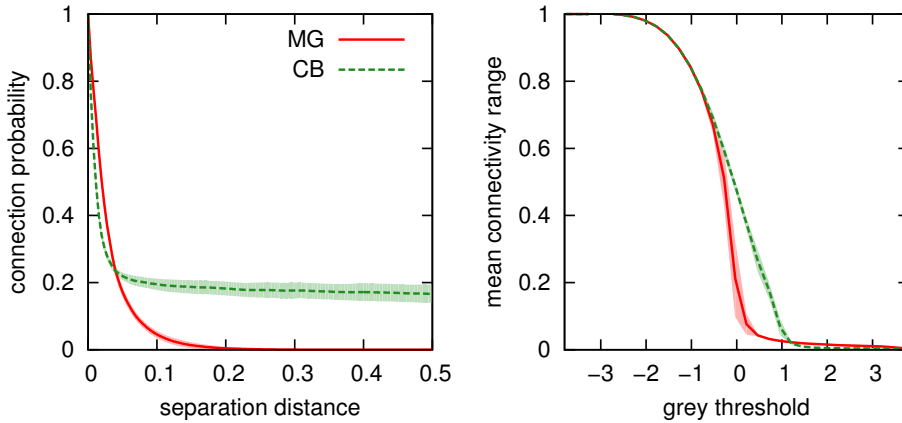


Figure 3.7: Left: pair connectivity function $\tau(h)$ for the MG and CB structure thresholded at the percolation threshold of the CB structure. Right: connectivity length as a function of grey threshold g_t . Shaded area represents standard deviation. Separation distance is scaled by the image size. Grey value is normalized by $(g - \langle g \rangle) \sigma_g^{-1}$.

Since the MG images do not percolate at the given threshold, $\tau(h)$ decays approximately exponentially (Allard and HERESIM Group, 1993; Western et al., 2001). For distances smaller than 2 correlation lengths (i.e. $0.05 \times$ image

size) the CB images have smaller $\tau(h)$ values than the MG structures simply because of their filigree geometry. However, $\tau(h)$ does not converge to zero but to the area fraction of the percolating cluster. Similar to the correlation length and the mean chord length, one can define a mean connectivity range by integrating $\tau(h)$ over all distances. This provides a single connectivity length as a function of grey threshold similar to the mean chord lengths presented above. The increased connectivity for the CB structure in the range between μ and $\mu + \sigma$ is clearly demonstrated in Fig. 3.7. This compares well with lower Euler numbers in that range. At higher thresholds g_t above $\mu + \sigma$, the connected bands fall apart evoking even smaller connectivity lengths than the compact objects of the standard MG structure. The connectivity function $\tau(h)$ must be evaluated within long ranges in order to fully capture large clusters. This makes it computationally inefficient for image reconstruction by global optimization. Therefore, it will not be used for stochastic reconstruction but only as a validation tool for structural connectivity. Despite of the benefits of a directional connectivity function reported by Western et al. (2001) we choose the omni-directional connectivity function, in order to stay comparable to the local percolation probability, that also accounts for any connection between opposite borders in one direction even if it is partly oriented backwards.

3.2 Stochastic reconstruction of structural heterogeneity

3.2.1 Simulated annealing

The stochastic reconstruction is performed via an extremely flexible global optimization method termed simulated annealing (Kirkpatrick et al., 1983; Yeong and Torquato, 1998). It is a Markov chain Monte Carlo method that is especially suited to incorporate information from different sources, both statistical (soft data) or measured (hard data) (Koltermann and Gorelick, 1996; Goovaerts, 1997; Deutsch and Journal, 1998). An energy function E is defined to express the difference between n predefined reference functions f provided by our reference images *ref* and those of the reconstructed (simulated) images *sim*. The structural connectivity metrics introduced in the last section

will serve as these predefined reference functions. These metrics are directly measured at the reference images, which contain the structural features that shall be reproduced. With $n > 1$ a multi-objective optimization problem is faced. As reference statistics f_n we choose the autocovariance function, the frequency distribution of local 2x2 configurations (i.e. all Minkowski functionals) as a function of grey threshold g_t and the four-directional two-phase chord length distribution also as a function of grey threshold g_t . The orthogonal and diagonal chords are evaluated separately to accommodate the impact of a different separation distance between adjacent pixels. Each of the statistics f_n has its own specific weight a_n that controls the relative importance for the optimization process. Thus, the energy function reads

$$E = \sum_n \sum_{g_t=0}^{g_t^{\max}} a_n [f_n^{\text{ref}}(g_t) - f_n^{\text{sim}}(g_t)]^2. \quad (3.2)$$

Since no hard data (i.e. measured values at specific locations) are used a purely unstructured random image serves as starting point for the reconstruction (initial image). Then single pixels are changed iteratively and the energy is recalculated. Thereby fast updating is aspired. This is possible for the reference metrics used here, since local changes can be attributed directly to the image statistics without recalculating the statistic for the entire domain. Goovaerts (1997) provides useful implementation details for fast updating using the example of semivariograms. Each pixel change is followed by a decision whether the perturbation is accepted according to the Metropolis rule (Metropolis et al., 1953).

$$p_k = \begin{cases} 1 & : \text{ if } \Delta E_k \leq 0 \\ e^{-\Delta E_k / T_m} & : \text{ if } \Delta E_k > 0 \end{cases} \quad (3.3)$$

If the energy decreases the change k is always accepted. However, if the energy increases it is only accepted with a certain probability. This prevents the optimization from getting stuck in local minima. The temperature T_m controls the acceptance probability and bestowed the term annealing upon the optimization method in analogy to controlled cooling of metals. An exponential cooling scheme,

$$T_m = T_0 e^{(\lambda-1)(m+1)}, \quad (3.4)$$

is used such that a global optimum is achieved as fast as possible. T_m is reduced by a factor λ by the end of every Markov chain m , that is after a predefined number of perturbations, which is either an acceptance target k_{acc} (e.g. as many accepted perturbations as pixels in the image) or a maximal number of attempts k_{max} (in the order of 10 times k_{acc}) (Deutsch and Journal, 1998). The starting temperature T_0 is adjusted to a desirable mean acceptance probability for the first Markov chain of $\langle p_{m_0} \rangle \approx 0.5$. Adapting λ dynamically to the rate of convergence allows for balance between fast convergence and avoidance of local minima (Ouenes et al., 1994; Talukdar et al., 2002).

$$\lambda = \text{Max} \left[\lambda_{\min}, \text{Min} \left(\lambda_{\max}, \frac{E_{\min}}{\langle E \rangle} \right) \right] \quad (3.5)$$

The minimum and maximum allowable reduction factors can be specified empirically to improve convergence, e.g. $\lambda_{\min} = 0.7$, $\lambda_{\max} = 0.95$. Reduction factors within that range are determined according to the ratio of mean energy $\langle E \rangle$ and minimal energy E_{\min} within the completed Markov chain. A stopping criteria of the annealing process is the number of Markov chains reaching k_{max} usually set to 2 or 3 (Deutsch and Journal, 1998).

3.2.2 Reconstruction details

The ensemble of possible realizations of simulated images all fulfilling the same reference statistics is typically enormous. By starting from different initial images of unstructured noise and choosing the locations of perturbations at random only some realizations of reconstructed images suffice to evenly sample that ensemble. Thirty images will be collected for each reconstruction model. To cover the possible variability within the reference heterogeneity model, the reference statistics for each reconstruction was obtained from a different realization of an MG or CB image.

All images have a size of 256x256 pixels with a grey scale of 8-bit. By equidistant classification the color space is reduced from 256 to 32 to reduce the computational effort of reconstruction, that is $g_{t_{max}} = 32$ in Eq. 3.2. Moreover, computation time is saved by reproducing distant-dependent metrics like the autocovariance and the chord length distribution only along principal directions and up to a maximum distance of about eight correlation lengths.

In case of bi-objective reconstruction the weights a_n were set to equalize the energy contribution of the two reference functions at the start of reconstruction. Periodic boundary conditions are assumed for reconstruction, i.e a chord might connect opposite boundaries of the image.

There are different schemes to choose a new grey value for each perturbation. Typically, a grey value is sampled randomly from a proposal distribution which is either uniform, Gaussian around the old value or equals the posterior frequency distribution as obtained from the reference image. Here, a rather heuristic scheme of a uniform proposal distribution within the grey value range of all neighbors is applied in order to achieve quick convergence. This definitely violates the ergodicity principle of sampling the entire parameter space (Besag et al., 1995) necessary to find the global optimum. But this is not critical since the exponential cooling scheme inhibits this as well and the interest is on near optimal solutions anyway.

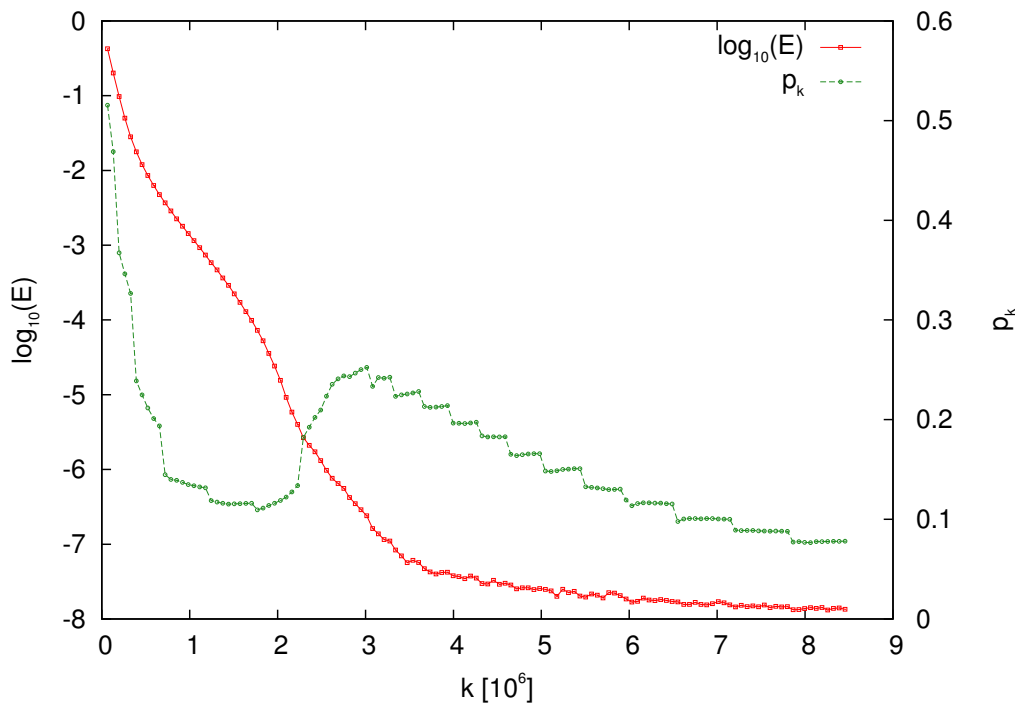


Figure 3.8: Evolution of energy $\log_{10}(E)$ and acceptance rate p_k for a single-objective optimization of Minkowski functions. Initial energy is set to $\log_{10}(E)=0$.

Figure 3.8 depicts the evolution of the energy E and the acceptance rate p_k for an optimization run, in which the frequency distribution of local 2×2

configurations (i.e. all Minkowski functionals) as a function of grey threshold g_t of a MG heterogeneity model is reconstructed. The initial energy is set to 1 and the values are plotted after periods of $k=65536$ iterations, i.e. the number of pixels in the image. The overall decrease in energy is about 8 orders of magnitude, which is achieved after roughly 8.5×10^6 iterations within 125 s computation time. The development of p_k demonstrates some interesting details. In the beginning, when p_k is high, only 2-3 periods suffice to reach the acceptance target $k_{acc}=65536$ in order to terminate one Markov chain m and adjust the temperature T_{m+1} for the next Markov chain. This is because the mean acceptance probability of the first Markov chain $\langle p_{m_0} \rangle$ is adjusted to 0.5. The temperature reduction effects an abrupt decrease in p_k . As the optimization evolves, more and more periods are necessary to reach k_{acc} in order to start a new Markov chain. Finally, k_{max} is reached sooner than k_{acc} , as p_k falls below 0.1 and the optimization ceases after two additional Markov chains. The characteristic increase in p_k between $2-3 \times 10^6$ iterations is a special feature of optimization of Minkowski functions and does not show up for the other structural connectivity metrics. However, overall energy reduction is comparable for all connectivity metrics.

3.3 Setup of numerical experiments

3.3.1 Stationary flow and transport

Structural heterogeneity manifests itself in many facets of which the interest in this study is structural connectivity. Any functional behavior of a heterogeneous field might serve as an additional test, whether differences in structural connectivity assessed by one of the structural connectivity metrics above directly translate into different functional behavior. This requires that other features of structural heterogeneity do not differ and that identical initial and boundary conditions are applied to the investigated process. Here, we adapt to previous studies that use a combination of flow and solute transport (Zinn and Harvey, 2003; Knudby and Carrera, 2005; Le Goc et al., 2010) to test for functional connectivity. The rationale is that the connectivity of high-K areas

might directly affect the amount of channeling, i.e. concentration of water flux in preferential flow paths, and as a consequence, also solute spreading.

A Miller similar medium introduced in Section 2.2 with a reference parameterization of $\theta_s = 0.32$, $\theta_g = 0.03$, $\alpha = 0.023 \text{ cm}^{-1}$, $n = 4.2$, $K_s = 2.22 \times 10^{-5} \text{ ms}^{-1}$, $\tau = 0.5$ and a standard deviation of log-scaling factors $\log(\chi)$ at $\sigma_\chi = 0.75$ will serve as a model domain for two different numerical experiments. The first experiment involves the MG and CB heterogeneity model only, whereas the second involves all heterogeneity models (MG, CB and MP) introduced in Section 3.1.1.

The first numerical experiment comprises a comparison of effective conductivity and solute arrival times in a stationary flow field for the two-dimensional MG and CB reference heterogeneity models, and their reconstructed counterparts. The experiment adapts to the two-step procedure of Zinn and Harvey (2003) so that results can be compared. In a first simulation step, saturated gravity flow is simulated with the Richards equation (Eq. 2.3). This is achieved by starting from a constant initial pressure head of $h_m = 0 \text{ cm}$ and applying constant Dirichlet boundary conditions of $h_m = 0 \text{ cm}$ at the upper and lower boundary. As a consequence, gravitation becomes the major driving force and the flow field will adapt to the paths of lowest flow resistance. At $h_m = 0 \text{ cm}$ the connected bands are saturated and are highly conductive, so that structural connectivity is expected to control the hydraulic response. The size of the domain is set to $1 \times 1 \text{ m}$. The simulations are performed by the $\mu\phi$ software package (Ippisch et al., 2006). The grid is implemented in a cell-centered finite volume scheme. The solver uses an implicit Euler scheme in time and a full upwinding scheme in space. An algebraic multigrid solver solves the linear equations. The time step is adapted automatically.

The stationary flux field for the realizations of the MG and CB heterogeneity model in Figure 3.1 are depicted in Figure 3.9 (top). The network of flow channels adapts to the underlying structure by local funneling of water into highly conductive regions. However, once a channel is established it persists over a large scale since it carries enough water to penetrate local spots of lower permeability (Roth, 1995; Le Goc et al., 2010).

In a second step, solute transport is modeled with the convection-dispersion equation (Eq. 2.4), without considering sorption and molecular diffusion. Ini-

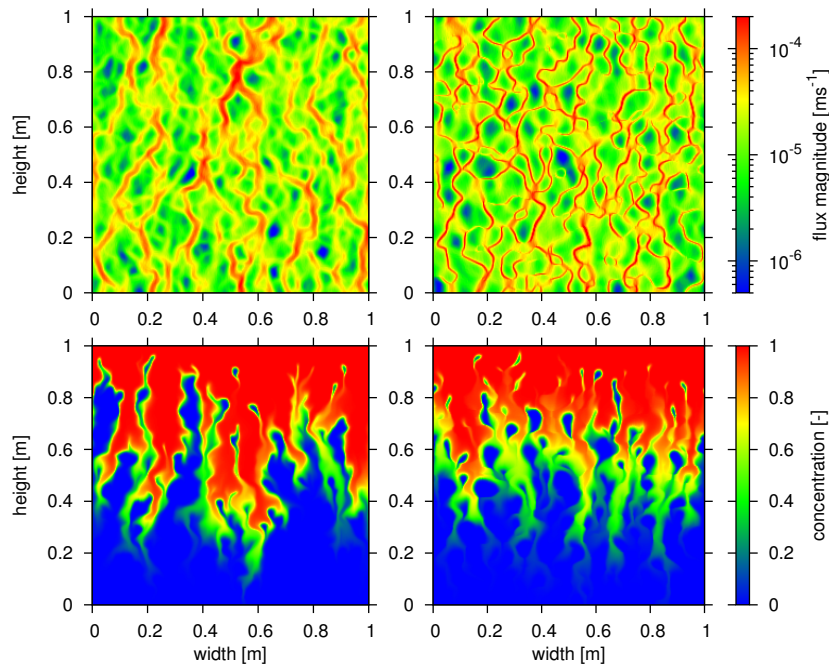


Figure 3.9: Magnitude of steady-state flux density (top) and solute concentration (bottom) after infiltration of 0.5 pore volumes of solute for one realization of the MG (left) and CB (right) heterogeneity model depicted in Fig. 3.1.

tially, the domains contains no solute. Then, a constant unit solute concentration is applied at the upper boundary as a step input so that solute enters the medium according to the local flux at the upper boundary and moves downwards like in Fig. 3.9 (bottom). A difference in K_{eff} between the two media is corrected for in Figure 3.9 by plotting the solute patterns for a certain solute volume that has entered the domain (0.5 pore volumes) instead of a certain point in time. Figure 3.9 indicates that the CB heterogeneity model evokes a higher density of preferential flow paths and as a consequence also less variability in the penetration depth of solute fingers. Finally, the output concentration at the lower boundary is monitored over time.

3.3.2 Infiltration

The second numerical experiment aims at the water dynamics during near-saturated infiltration into a previously dry soil. Initially hydraulic equilibrium prevails with a hydraulic head of $h = -100$ cm through out the entire domain. A free drainage boundary condition is applied to the lower boundary, evoking

a unit gradient across the boundary. At the upper boundary a Neumann-type condition (flux boundary condition) is applied, with a constant infiltration rate of $j_0 = 2.22 \times 10^{-5} \text{ ms}^{-1}$. This value corresponds to the saturated hydraulic conductivity of the reference parameterization of the Miller medium. The type of the upper boundary condition is important. In the first experiment a Dirichlet-type boundary condition is used to impose a head gradient between opposite borders, in order to investigate the impact of connectivity on effective hydraulic behavior at saturation. This choice has been made to stay comparable to other studies with a focus on groundwater hydrology, where this is an appropriate adaptation to natural conditions. In vadose zone hydrology, however, the upper boundary is controlled by the atmosphere and it is governed by fluxes such as precipitation and evaporation. Due to a constant head at the upper boundary water would enter the domain proportionally to local K values and a higher connectivity of high-K zones would result in an increased effective permeability (Sánchez-Vila et al., 1996; Wen and Gómez-Hernández, 1998; Zinn and Harvey, 2003; Knudby and Carrera, 2005). With a constant flux boundary condition, however, water is forced to enter the soil uniformly and local pressure heads near the surface adapt accordingly. As the flux rate is fixed, the effective permeability must not change with a modified connectivity but the hydraulic head is expected to adapt.

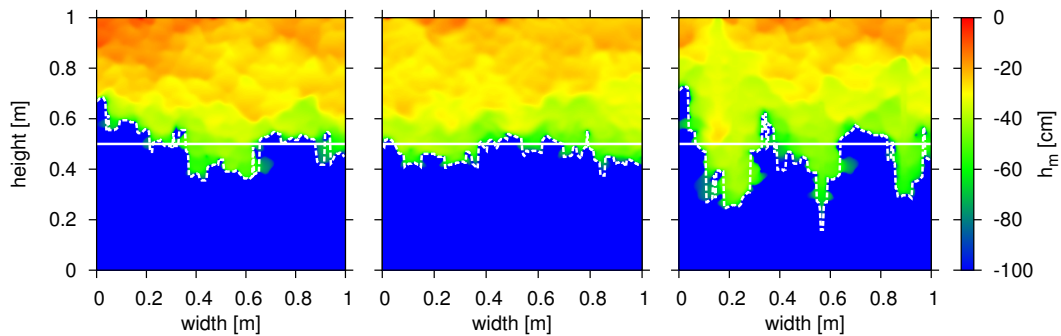


Figure 3.10: Pressure head after 70 min of infiltration with $j_0 = 2.22 \times 10^{-5} \text{ ms}^{-1}$. The underlying heterogeneity fields correspond to Fig. 3.1 (MG-left, CB-middle, MP-right). The white lines mark the depth in which the state variables are averaged (solid) and the location of the maximum gradient in flow direction for each pixel column (dashed).

Figure 3.10 highlights differences in the morphology of the infiltration front between the MG, CB and MP structures in Figure 3.1 by means of pressure heads after 70 min of infiltration. For further analysis water content θ , pressure

head h_m and vertical flux density j_z at every pixel location along the control line in the middle of the profile (solid line) is monitored over time and averaged according to Section 2.3. Moreover, the location of the front is estimated via the maximum pressure gradient in flow direction for each pixel column (dashed lines).

3.4 Functional connectivity metrics

3.4.1 Channeling and solute spreading

The flux and solute patterns in Figure 3.9 already demonstrated an impact of structural connectivity on local patterns of water and solute displacement. On top of that, structural connectivity also affects the effective behavior of the entire domain as can be seen from the solute breakthrough curves in Figure 3.11. Solute transport in the CB structure differs from the MG image in a pronounced early arrival. Evidently, the increased structural connectivity in the CB heterogeneity model leads to an increased effective hydraulic conductivity that merely shifts the breakthrough curve towards earlier arrival times. In addition, the slope of concentration increase is higher, which is also reflected by the peak and the skewness of concentration change.

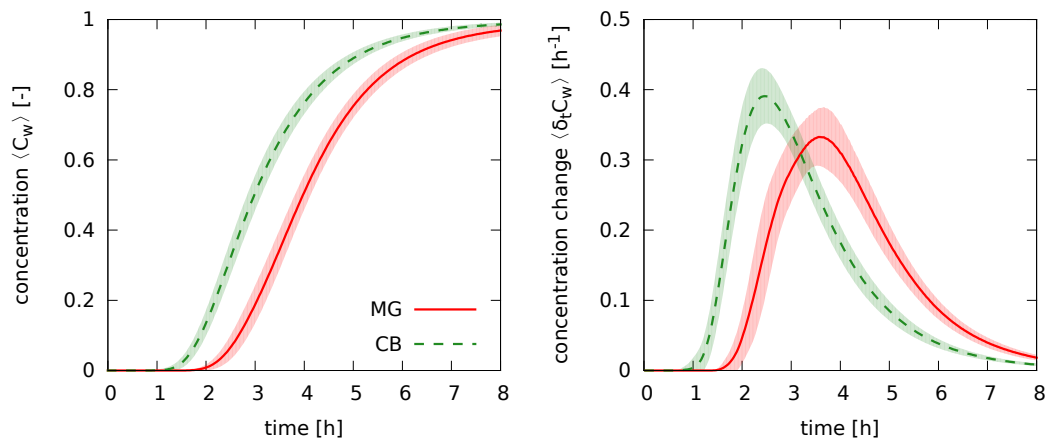


Figure 3.11: Comparison of breakthrough curves (left) for 30 realizations of the MG and CB heterogeneity model and its derivative with respect to time (right). Shaded areas represent standard deviation

It is appealing too condense all information on stationary flow and transport behavior into a few indicator values that can be easily compared for different heterogeneity models. Knudby and Carrera (2005) surveyed various candidates for flow connectivity and transport connectivity metrics alongside structural connectivity metrics and observed different responses of flow and transport connectivity to changes in structural connectivity. Specifically, flow connectivity indicators are more controlled by the continuity of preferential flow paths whereas transport connectivity is seemingly more controlled by the thickness of these paths (Knudby and Carrera, 2006). The following indicators proved to be best suited to describe flow connectivity and transport connectivity and have been used in others studies since (Le Goc et al., 2010; Bianchi et al., 2011):

$$CF = K_{\text{eff}}/K_{\text{geom}} \quad (3.6)$$

$$CT = t_{\text{ave}}/t_5 \quad (3.7)$$

where K_{eff} is the effective saturated conductivity as obtained from the measured flux rate and the imposed pressure gradient between opposite borders. The subscript _s for saturated is omitted here. K_{geom} is the geometric mean of local K values, t_{ave} is the average solute arrival time as obtained from the first moment of a break through curve and t_5 is the time when 5% of the applied solute pulse has arrived the outlet. Note that t_5 and t_{ave} in Eq. 3.7 have to be adjusted to a step input, since they are originally defined for a solute pulse. CF takes advantage of Matheron's theorem (Matheron, 1967) for saturated media, stating that effective permeability of a Multigaussian permeability field equals the geometric mean of local permeabilities. Hence, CF values higher than one indicate an increased effective permeability as compared to a frequently used reference case, inferring a tendency towards preferential flow. CT also relates an estimator of preferential transport with a suitable reference. It reflects the ratio of early arrival to the mean arrival of a solute. The first is only controlled by the fastest proportion of a solute plume, whereas the second is mainly affected by K_{eff} . Swapping the numerator and denominator ensures an increase of CT with accelerated early arrival.

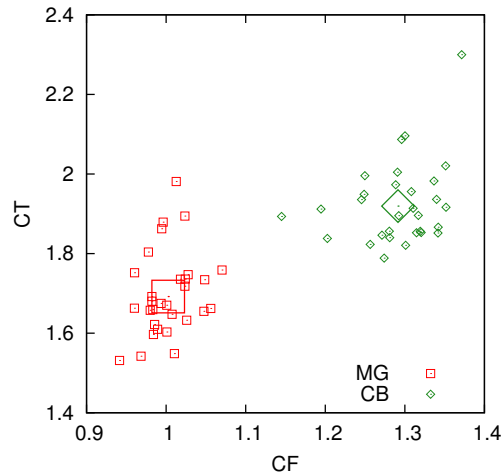


Figure 3.12: Comparison of flow and transport connectivity indicators CF and CT for 30 realizations of the MG and CB structure. Big symbols represent averages.

Fig. 3.12 depicts CT and CF for 30 realizations of the MG and a CB heterogeneity model. On average, the MG heterogeneity model has an CF of 1 which is in line with analytical predictions and a CT of 1.69. The CB model evokes an increase in CF by roughly 30% due to a higher K_{eff} value. Moreover, a CT value at 1.91 indicates a slightly more pronounced early solute arrival as compared to bulk arrival. The increase in CF due to a CB transform is well in line with previous findings (Zinn and Harvey, 2003; Knudby and Carrera, 2005; Le Goc et al., 2010), whereas the increase in CT is contradictory to the decrease or indifference reported previously (Knudby and Carrera, 2005; Le Goc et al., 2010). This however, stems from the fact that the present MG heterogeneity model is already adjusted to the smaller correlation length of the CB heterogeneity model which also reduces CT for MG model, whereas in the other studies it was not.

3.4.2 Hydraulic non-equilibrium

In the infiltration study the local state variables θ and h_m are not constant in time anymore like in the stationary flow simulations, but change suddenly when the infiltration front traverses. The passage of the infiltration front entails a state change from low θ and h_m values to high θ and h_m values and the specific dynamics is governed by local material properties. This dynamics can be thought of as a trajectory within the (θ, h_m) -space. Since θ and

h_m are always in local equilibrium, the trajectory will always lie on top of a well-defined water retention curve resulting from the given reference parameterization and a given Miller scaling factor at that location. That is to say, a dot in Fig. 3.13(left) will never leave the trajectory of a given scaling factor χ represented by different shades of grey. However, the focus is not on local states but on an effective state representing an entire depth. Thus, θ and h_m need to be averaged according to the equations in Section 2.3. Fig. 3.13(left) depicts all local (θ, h_m) -pairs within the control line of the MG structure in Fig. 3.10 after 70 min of infiltration. Since the infiltration front has traversed the control line only partly, some locations are already wetted, whereas others still remain at their initial state. As a consequence, the soil in that depth is said to be in hydraulic non-equilibrium. In this case, averaging of pressure head becomes a delicate issue and will lead to different results of $\langle h_m \rangle$ depending on the method applied.

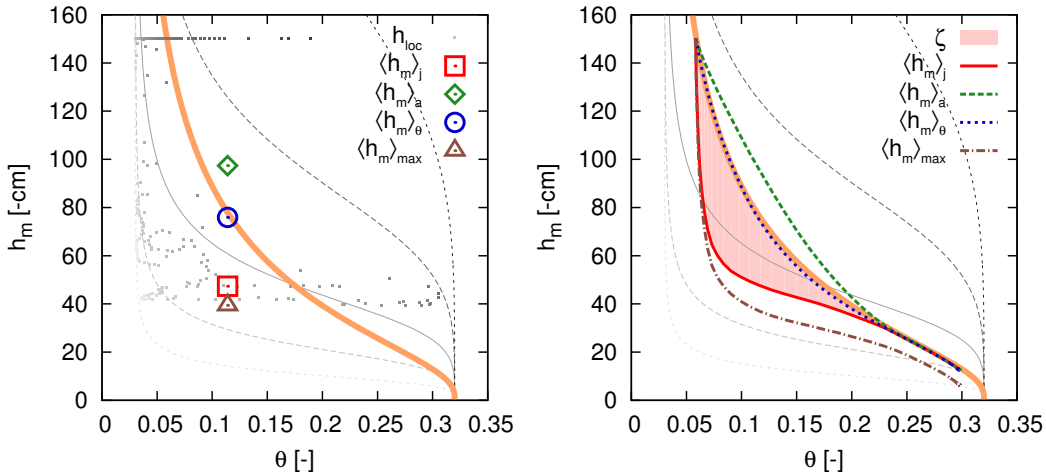


Figure 3.13: Evolution of averaged pressure heads at a horizontal control line at the passage of an infiltration front. Values represent the mean of 30 realizations of a MG heterogeneity model. The notation is according to eq. 2.6-3.8. Meaning of other curves is according to Fig. 2.1

Fig. 3.13(right) depicts the mean $(\langle \theta \rangle, \langle h_m \rangle)$ -trajectories of 30 MG realizations for the entire simulation period. Depending on the averaging procedure for h_m we find different trajectories within the (θ, h_m) -space during the passage of an infiltration front. All trajectories start at a certain point on the thick orange effective water retention curve corresponding to the initial condi-

tions at hydraulic equilibrium in the depth of the control line. During passage of the infiltration front the curves diverge due to the different calculation of $\langle h_m \rangle$. Subsequently, the trajectories rejoin when a new steady-state flux is reached behind the front. The θ -weighted pressure heads remain close to the effective water characteristic, suggesting that in spite of soil heterogeneity the infiltration front moves uniformly like in piston flow. The front is of course irregular and the indifference arises because the dynamics of weighting factors adapt to the equilibrium water characteristic. At arithmetic averaging the contribution of every local h_m to the mean remains constant. Thus, at the early arrival of the front a steep increase in pressure heads is smeared out by unchanged pressure heads at other location in that depth. At flux-weighted averaging $\sum j$ is zero at hydraulic equilibrium, so that $\langle h_m \rangle_j$ is actually not defined initially. At the onset of non-equilibrium, only those locations where the front has traversed the control line exclusively contribute to the average, leading to a steep increase in pressure heads. This effects an apparent delay in $\langle \theta \rangle$ as compared to $\langle h_m \rangle$. The behavior of the maximum pressure head is quite similar at the beginning. However, $\langle h_m \rangle_{max}$ does not relax towards the equilibrium water retention curve, whereas $\langle h_m \rangle_j$ does, as soon as the entire front has passed the control line. From this observations it can be concluded that the flux-weighted pressure head $\langle h_m \rangle_j$ is superior to all other averaged pressure heads for two reasons: (i) it is suited to describe hydraulic non-equilibrium as the front passes and (ii) it relaxes to the equilibrium water retention curve under steady-state conditions. Furthermore, this macroscopic behavior is in accordance with experimental observation where it has frequently been found that the water content is lagging behind the pressure head (Topp et al., 1967; Vachaud et al., 1972; Wildenschild et al., 2001). As pointed out in Figure 3.13, $\langle h_m \rangle_j$ also has the merit that the magnitude of non-equilibrium ζ may be quantified as the area enclosed by the upscaled non-equilibrium and equilibrium water characteristic.

$$\zeta = \int_{\theta} (\langle h_m \rangle_j - h_m^{\text{eq}}(\langle \theta \rangle)) d\langle \theta \rangle \quad (3.8)$$

where $h_m^{\text{eq}}(\langle \theta \rangle)$ is the pressure head that would adjust to the actual water content at hydraulic equilibrium, including hydrostatic equilibrium as a special case. The integral is solved by numerical integration over all times steps

in which $\langle h_m \rangle_j$ and $h_m^{\text{eq}}(\langle \theta \rangle)$ deviate. For this purpose rescaling of hydraulic non-equilibrium is necessary, due to the following reason: The frequency distribution of scaling factors along the control line of each realization is not perfectly log-normal. Therefore, the start and convergence point of the dynamic water retention curve do not superimpose with the equilibrium curve as defined for the entire domain. As a consequence, the integration limits for hydraulic non-equilibrium are ill-defined. By rescaling, the state variables are corrected towards values that would have appeared for $\log(\chi) \sim N(0, \sigma_\chi)$. This rescaling is also denoted as functional normalization (Vereecken et al., 2007) and is explained in detail in Appendix A. When pressure heads are recalculated into matric potentials and multiplied with the horizontal cross sectional area A passed by the infiltration front, the physical meaning of the resulting quantity $\zeta \cdot A$ might be interpreted as the energy per infiltration depth [J/m] corresponding to the amount of viscous energy dissipation due to funneling of water in high flux channels (Kleidon and Schymanski, 2008; Zehe et al., 2010). Consequently, ζ may serve as a functional connectivity metrics that quantifies the degree of channeling due to structural heterogeneity. It is zero for a uniform front propagation and increases with flux concentration in channels that causes a delayed relaxation of head gradients.

Chapter 4

Results

4.1 Stochastic Reconstruction

4.1.1 Single- and Multi-objective optimization

In Section 3.2 simulated annealing has been introduced as an optimization method to stochastically reconstruct heterogeneity fields that obey a given structural connectivity metric. Several of these structural connectivity metrics have been introduced in Section 3.1.2. In the following we will visually compare the reconstruction results of four different structural connectivity metric: the autocovariance as a simple two-point statistic (2p) and various multi-point statistics which are the Minkowski functions (mf), the chord length distribution (cl) and a combination of mf and cl (mp). The first three can be denoted as single-objective optimization since only one connectivity metric has been reproduced, whereas the last is a multi-objective optimization problem. In fact, also the 2p and cl reconstructions call for a multi-objective optimization, since the frequency distribution of grey values (histogram) also has to be reproduced, whereas it is directly included in the Minkowski functions (mf) via the area fraction of the foreground phase in every level set.

Only the MP and the CB heterogeneity models are involved as reference images for stochastic reconstruction, since they fulfill the requirements to be (i) isotropic and to (ii) have characteristic scales much smaller than the image size. The MP heterogeneity in turn is excluded, because the vertical macropores span half the image length, which would call for expensive optimization of

long-range correlation and chords lengths. Moreover, they introduce some anisotropy, which is not the focus of this study.

As Figure 4.1 indicates, the two-point statistics serve as a thorough description of the MG structure. The reconstruction result for the CB structure is statistically nearly identical, however, connectivity features are not reproduced for the reasons discussed previously. The two multi-point statistics that we use as reference statistics for reconstruction are sensitive to different structural properties. While Minkowski functionals including the Euler number address the topology of a complex structure, this is not the case for chord length distributions. In contrast, the chord length distributions describes the size distribution of clusters, while the Minkowski functionals as integral properties are not sensitive to this feature. These differences become evident in Figure 4.1. There the results of reconstruction are compared for each type of statistics supplemented with a combination of both. Matching only the Minkowski functionals obviously leaves to much freedom for the size of the evolving objects, since the compact 2x2 statistic contains no information on spatial correlation of the reference heterogeneity model. In contrast, reproducing the chord length distribution for both phases at all thresholds in four directions (horizontal, vertical, 2 diagonals) adequately reproduces the spatial correlation as well as the elongated morphology of connected bands. Note however, that the bands appear more fragmented than in the reference image at least from a visual point of view. Another morphological deviation from the reference images are some rectilinear structures caused by the reconstruction process. More directional artifacts emerge when the diagonal chord lengths are not considered. Therefore, the two-fold increase in computational cost by reconstructing chord lengths in four direction is justified (Čapek et al., 2009). Note that conditioning the reconstruction solely on the chord length distribution of the background phase leads to comparably well reconstruction results, while the reconstruction of connected bands completely fails if only the foreground is used. This implies that the chord length distribution of the foreground phase (the bands) does indeed not contribute too much additional morphological information as it has been previously stated (Antoine et al., 2009). Finally, the combination of both multi-point statistics leads to an improved reconstruction which resembles the reference image visually.

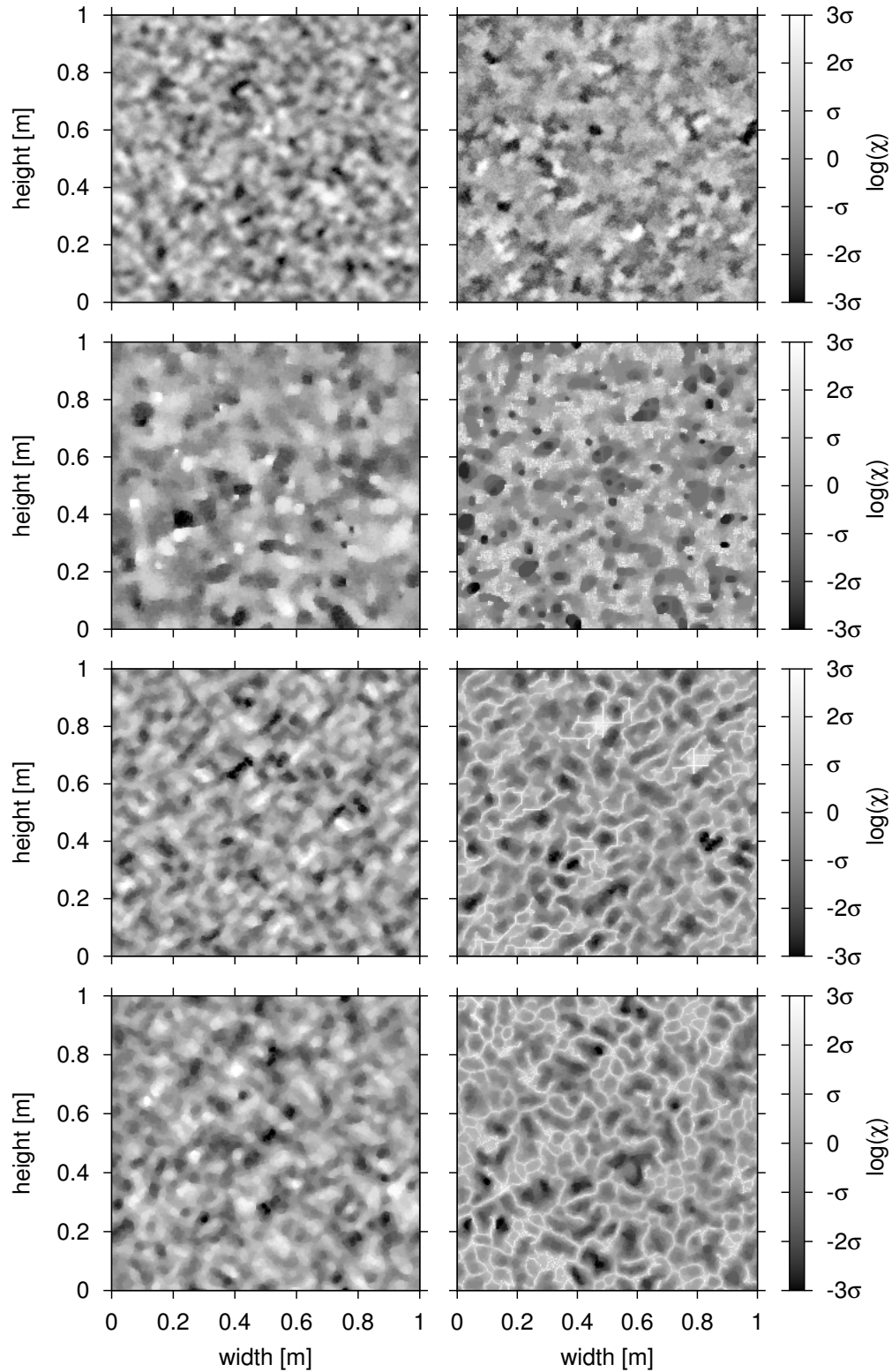


Figure 4.1: One realization of stochastic reconstruction of a MG heterogeneity model (left) and a CB heterogeneity model (right) with four different structural connectivity metrics. From top to bottom: autocovariance (2p), Minkowski functions (mf), chord length distribution (cl) and combined multi-point statistics (mp).

4.1.2 Estimators of Structural Connectivity

Local Percolation Probability

Any connectivity metric that was not included in the reconstruction process and that is deemed to contain some valuable structure information can be used as a test statistic for validation. Local percolation probability is especially suited to test for structural connectivity. It provides a comprehensive description of connectivity which has not been used as a reference statistic for reconstruction. The binary images required to calculate local percolation probabilities were obtained by choosing the grey threshold such that the Euler number is zero. The resulting binary images are deemed to be most sensitive to connectivity features. In Figure 4.2 (left) we compare the local percolation probability of the reference MG image, with those from simulated images matching two-point and multi-point statistics.

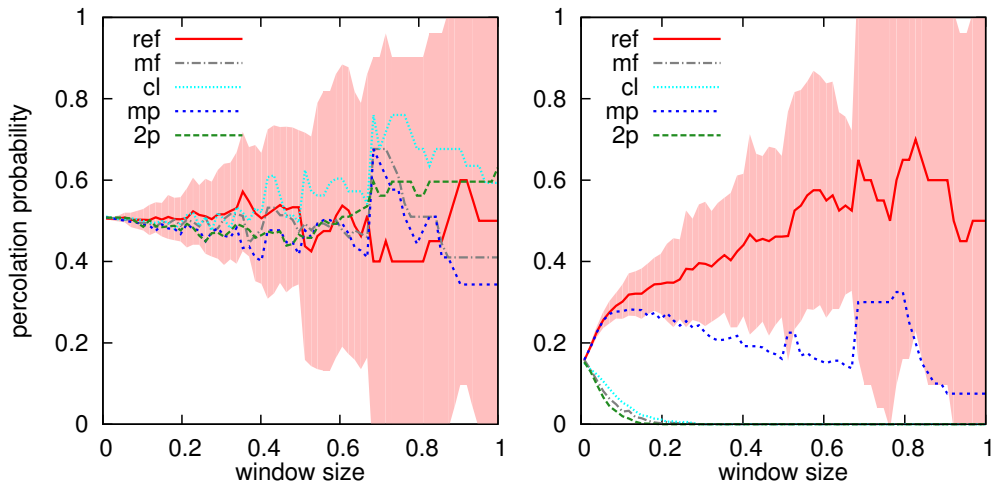


Figure 4.2: Local percolation probability for 30 realizations of MG structures (left) and the CB structures (right) for binary images at the specific percolation threshold of the MG and CB images (ref-reference, mf-Minkowski functions, cl-chord length distributions, mp-combined multi-point statistics, 2p-two-point statistics). Shaded area represents standard deviation of the reference set. Window size is scaled by the image length.

In case of the MG heterogeneity model, local percolation properties of all reconstructed images are in good agreement with the reference images. The local percolation properties for the CB image in Figure 4.2 (right) turns out to differ considerably. Again the starting point is located at the area fraction of pixels brighter than the percolation threshold. The reconstructed images based

on two-point statistics (2p) or individual multi-point statistics (mf,cl) quickly drop to completely non-percolating states as soon as the window size gets bigger than the length of the isolated objects. The combination of Minkowski functions and chord lengths significantly (mp) improves the reproduction of percolation properties. The fraction of percolating windows compares well for window sizes up to 1/10 of the domain size corresponding to 4 correlation lengths but then decreases to a non-zero fraction significantly smaller than the reference value.

Pair connectivity function

Figure 4.3 (left) shows the good reconstruction of mean connectivity ranges for reconstructed MG images using multi-point statistics as well as two-point statistics.

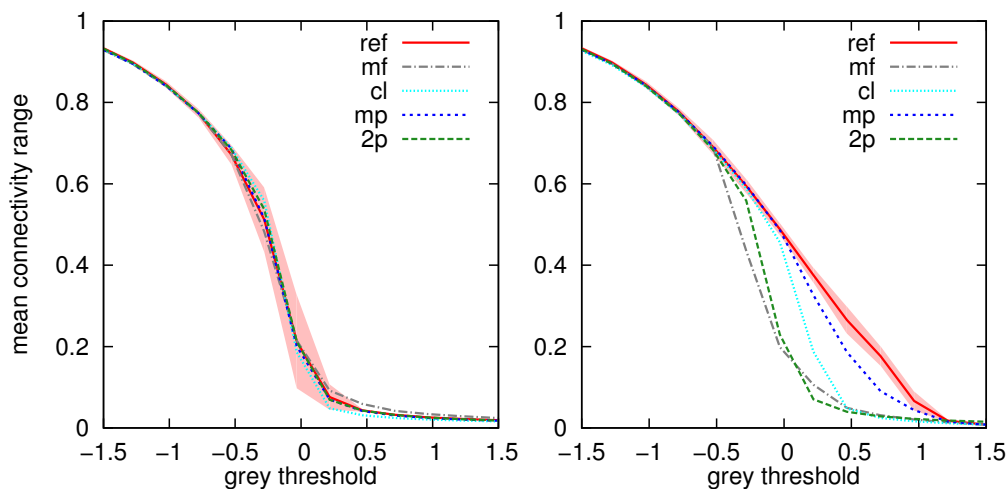


Figure 4.3: Mean connectivity range as a function of grey value threshold for reference and reconstructed images of the MG structure. Notation is according to the Figure 4.2 . Note the reduced abscissa for thresholds.

This is different for the CB structure shown in Figure 4.3 (right) where two-point statistics is clearly not sensitive to long range connectivity. This is also true for reconstructions based on Minkowski functions or chord lengths only. The combination of both, however leads to a significantly better reproduction of connectivity length. Yet, the mean connectivity length is lower than the reference values in a small interval with the highest discrepancy around the percolation threshold.

4.2 Steady-state flow and transport

4.2.1 Estimators of functional connectivity

Now that different capability of various structural connectivity metrics to reproduce long-range connectivity of high-K zones has been identified, the question arises whether this also translates to the functional connectivity metrics CF and CT. That is to ask: Does the reconstructed heterogeneity model reproduce effective flow and transport behavior of the reference heterogeneity models? If this is the case, then the specific structural connectivity metric used for stochastic reconstruction is deemed to capture structural connectivity sufficiently well. In turn, if the resulting images from stochastic reconstruction reproduce only one or none of the processes well then the structural features that govern functional connectivity are insufficiently captured.

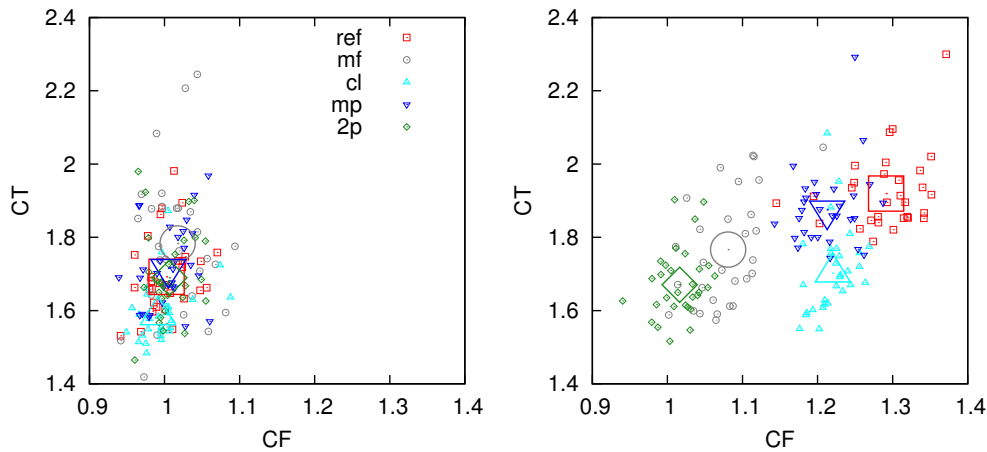


Figure 4.4: Comparison of flow and transport connectivity indicators CF and CT between the reference heterogeneity model and the reconstructions for the MG structure (left) and the same for the CB structure (right): reference (ref), semivariogram (2p), Minkowski functions (mf), chord length distribution (cl) and combined multi-point statistics (mp).

To this end, we simulate the steady-state flow and transport experiments for 30 realizations generated from single- and multi-objective stochastic reconstruction, calculate the indicators of flow and transport connectivity, CF and CT, that were introduced in Section 3.4 and compare them with the indicator values of the reference heterogeneity models. Figure 4.4 depicts the CF and CT value of every realization from the reference model and the various reconstructions for the MG heterogeneity model (left) and the CB heterogeneity

model (right). For the MG heterogeneity model on the left flow connectivity, as estimated by the CF indicator, is reproduced well by all structural connectivity metrics. The fact that on average all reconstructed heterogeneity models have a CF value close to one, suggests that they all fulfill the premise of Matheron's theorem (Matheron, 1967) which is the symmetry of indicator variograms around the mean. That is to say, they all behave Multigaussian. In addition, the CT indicator is well reproduced by the 2p heterogeneity model reconstructed from two-point statistics. In fact, the reference MG images have been generated from the histogram and the autocovariance function only, which then has been reconstructed from the 2p -statistic again. Any difference between the two CT averages, can therefore only be a consequence of poor reconstruction or too few realizations. On average, the mf heterogeneity fields reconstructed from Minkowski functions exhibit a slight overestimation of CT values. Evidently, spatial correlation is not well addressed by a compact four-point statistic (mf) which inevitably leads to more spatial disorder resulting in increased solute spreading. Spatial correlation is assessed indirectly by a chord length distribution and yet on average the cl heterogeneity fields exhibits slightly to low CT values, which suggests that the structural heterogeneity tends to be too regular. Finally, the combination of Minkowski functions and chord length distribution in the mp heterogeneity model results in equal CT values like the reference and the 2p heterogeneity model.

The right hand side of Figure 4.4 depicts the flow and transport connectivity indicators for the reference and reconstructed CB models. On average, none of the reconstructed models matches the CF and CT values of the reference. The 2p heterogeneity model yields the poorest match, since it remains at values observed for the MG reference. The Minkowski functions (mf) lead to a small increase in both CT and CF as compared to two-point statistics (2p). The chord length distribution (cl) especially improves the CF values, indicating channelized, preferential flow. The combined multi-point statistic (mp) leads to an equally good reproduction flow connectivity and the best match in solute spreading behavior indicated by CT.

4.2.2 Solute breakthrough curves

To substantiate the findings of the functional connectivity indicators CF and CT, we compare the mean breakthrough curves of 30 realizations for each reference structure and each reconstruction model. In Figure 4.5 (left) the cumulative breakthrough curves of the standard MG structure is depicted together with those of the reconstructed fields.

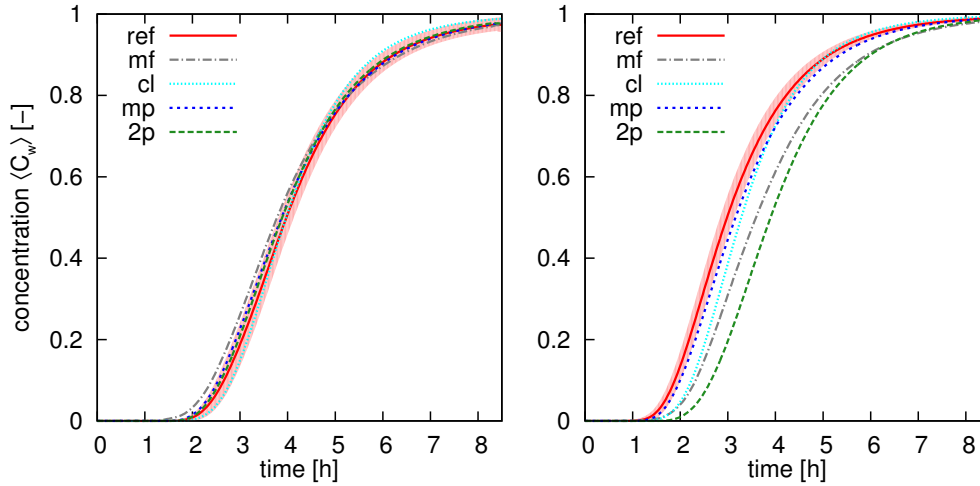


Figure 4.5: Breakthrough curve for 30 realizations of the reference MG (left) and CB (right) structures and the mean breakthrough curve of the corresponding reconstructions. Shaded area represents standard deviation in the reference break through curve. Notation is according to the last figures.

There are almost no differences in transport behavior between the reference MG structure and the reconstructed fields using two-point statistics (2p). The combined multi-point statistics (mp) exhibit almost identical breakthrough curves. The reconstruction from Minkowski functions (mf) yields too high early solute arrival, whereas the late time tailing behavior is adequately reproduced. The reconstructions from chord length distribution (cl) indeed exhibits a slightly too low dispersivity, which already has been deduced from the CT indicators.

The transport behavior of the CB images and their reconstructions are compared in Figure 4.5 (right). The solute arrival for the two-point reconstructions (2p) is clearly delayed. The extension towards Minkowski functions (mf) or chord lengths (cl) both improves the results. However, a good agreement is only obtained by the combination of both morphological descriptors. The dif-

ference to the reference structure becomes as small as the variability among different realizations. This implies that transport behavior can be reasonably well predicted from Minkowski functions and two-phase four-directional chord length distributions.

4.3 Hydraulic non-equilibrium during infiltration

4.3.1 Heterogeneity effects on front propagation

The numerical infiltration experiment comprises hydrostatic equilibrium ($h = -100$ cm) at the beginning, a free drainage condition at the lower boundary and a constant irrigation rate ($j_0 = 2.22 \times 10^5 \text{ ms}^{-1}$) at the upper boundary that equals the reference saturated conductivity of the Miller medium. The flux across the horizontal transect at 0.5 m depth as a function of time is depicted in Fig. 4.6.

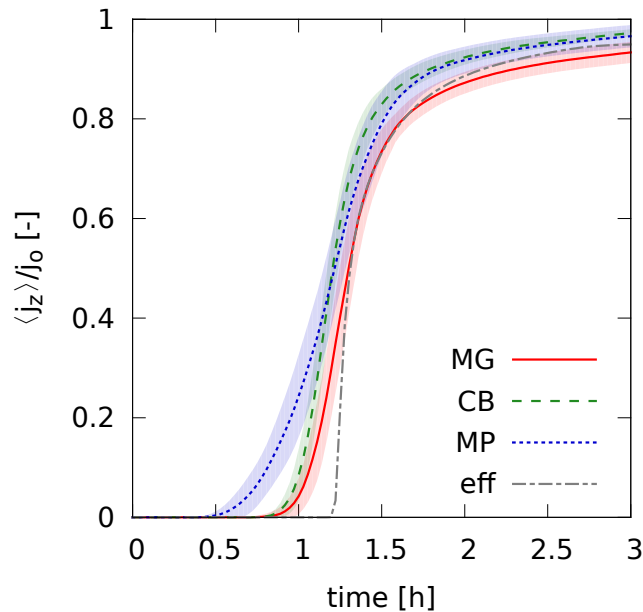


Figure 4.6: Evolution of mean vertical flux density at the control line for the different heterogeneity models (MG- Multigaussian, CB- connected bands, MP - macropores) and a homogeneous field with effective parametrization (eff). Mean (line) and standard deviation (shaded area) of 30 realizations each.

Due to the flux BC the steady-state flux value is equal for all heterogeneity models and is dictated by the boundary condition. However, stationary con-

ditions indicated by $\langle j_z \rangle / j_0 = 1$ have not yet been established after 3 h. This is partly due to the free drainage condition at the lower boundary that decelerates the dynamics towards the steady state once the front has approached the lower boundary. The onset of flux is sooner, when the structure evokes funneling of water into channels of fast flow. Of course this is the case for every heterogeneity model as compared to the homogeneous reference case and little surprisingly it is most pronounced in presence of macropores. However, it is interesting to see that the temporal difference in early onset of flux between the Multigaussian and the connected band heterogeneity model is negligible. Yet, the two heterogeneity models differ in that the flux increase over time is steeper in the presence of connected bands. Without further information it is unclear whether this stems from different front morphologies, different front speeds or different pressure gradients across the front. To disentangle these different sources one has to look at the two determining factors of flux separately. According to the Buckingham-Darcy law for one-dimensional flow,

$$j_z = -K(\theta) \left(\frac{dh_m}{dz} + 1 \right) \quad (4.1)$$

these are the hydraulic gradient ($dh_m/dz + 1$) and the unsaturated conductivity $K(\theta)$. The dynamics of these two factors are depicted in Figure 4.7 in terms of averaged, effective values at the control line.

The left hand side shows the averaged, vertical gradient in hydraulic head $\langle dh_m/dz + 1 \rangle$ either obtained from j_z -weighted averages of hydraulic head (solid lines) or from θ -weighted averages (dashed lines). The j_z -weighted mean hydraulic gradients are supposed to be most sensitive to early front arrival since the contribution of no flow areas along the transect remain zero. Consequently, the peak gradients coincide with the initiation of flux in Figure 4.6. For the θ -weighted averages, in turn, the peak gradients coincide with the main passage of the front. Figure 4.7 demonstrates that the steeper flux increase in the CB structure as compared to the MG structure is not evoked by higher hydraulic gradients. Hence, Eq. 4.1 implies that $\langle \theta \rangle$ and thus $K(\theta)$ has to increase faster. This is corroborated by the right hand side of Figure 4.7. The early peak gradient and the early increase in $\langle \theta \rangle$ by the MP heterogeneity model again demonstrates that the control depth is reached much earlier by the infiltration front in presence of vertical macropores.

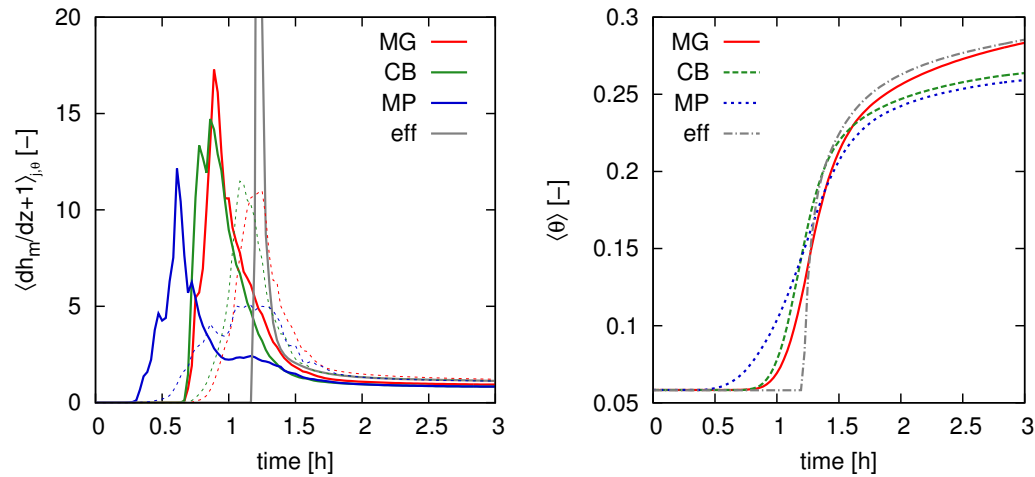


Figure 4.7: Left: Evolution of averaged, vertical gradients in hydraulic head $\langle dh_m/dz+1 \rangle_{j_z}$ at the control line for the different heterogeneity models (MG- Multigaussian, CB- connected bands, MP - macropores) and a homogeneous field with reference parametrization (eff). Solid (dotted) lines represent j_z -weighted (θ -weighted) averages. Right: Evolution of averaged water contents $\langle \theta \rangle$ for the same heterogeneity models (30 realizations each).

4.3.2 Heterogeneity effects on hydraulic non-equilibrium

Figure 4.8 demonstrates that the CB heterogeneity and the MP heterogeneity influence hydraulic non-equilibrium towards different directions.

Taking the MG model behavior as a reference, elongated macropores provoke an increased non-equilibrium behavior whereas isotropically connected bands tend to reduce it. The proper explanation may lie in the flux patterns at the front depicted in Figure 4.9. The CB heterogeneity evokes the highest density of high-flux channels and because of their omni-directional orientation also the best lateral redistribution of water, causing the flux to be relatively high everywhere at the front. The MP model in turn produces distinct funneling of water into a few isolated high-K channels. A high concentration of flux in the tip of the front hinders the soil to quickly saturate everywhere so that mean saturation is lowest at a given transient pressure. When the front has passed the control line entirely, flux-weighted pressure heads arrive at the equilibrium retention curve for all heterogeneity models. At this last stage pressure heads still increase to some extent until every heterogeneity model ceases at a different steady-state value. This last-stage behavior could have also been modeled adequately with intrinsic phase averages $\langle h_m \rangle_\theta$. At steady state a

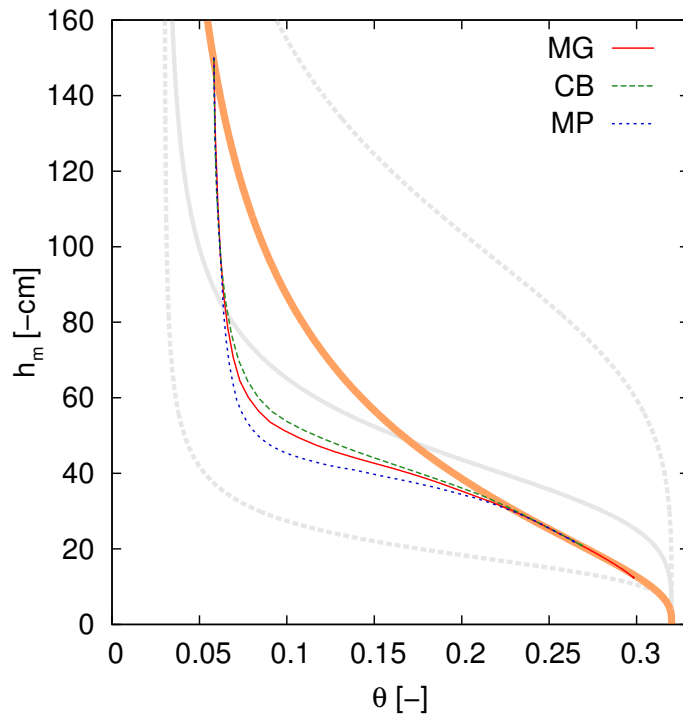


Figure 4.8: Evolution of state variables at the control line for the different heterogeneity models (MG- Multigaussian, CB- connected bands, MP - macropores), plotted as the mean of 30 realizations each.

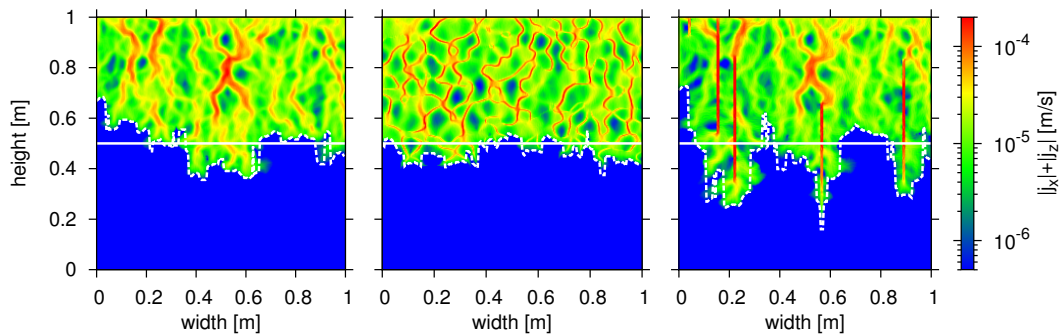


Figure 4.9: Magnitude of flux density after 70 min of infiltration with $j_0 = 2.22 \times 10^{-5} \text{ ms}^{-1}$. The underlying heterogeneity fields correspond to Fig. 3.1 (MG-left, CB-middle, MP-right). The white lines mark the depth in which the state variables are averaged (solid) and the location of the maximum gradient in flow direction for each pixel column (dashed).

particular effect of the applied flux BC appears: A well-connected structure may remain less saturated in order to allow for the same flux, as compared to a poorly connected structure.

4.3.3 Heterogeneity effects front morphology

Until now, hydraulic non-equilibrium has only been elaborated with respect to state variables. A logical supplement may lie in spatial information on non-equilibrium, particularly in the shape of the infiltration front. Fig. 3.10 depicts the position of the front after 70 min of infiltration for one model realization each. It is determined as the location of maximum head gradient in downward direction along every pixel column $\langle dh_m/dz+1 \rangle_{max}$. A simple indicator of front irregularity may be calculated as the standard deviation of front position $\sigma_{\langle z \rangle}$ around the mean front depth $\langle z \rangle = \langle z_{\langle dh_m/dz+1 \rangle_{max}} \rangle$, as it is done in Figure 4.10.

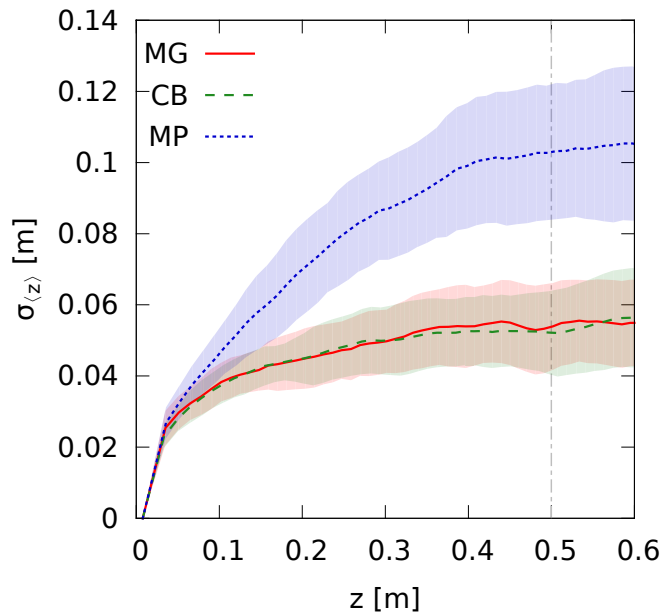


Figure 4.10: Front spreading for different heterogeneity models (MG,CB,MP) expressed as the standard deviation of locations with maximum vertical head gradient plotted against mean depth of the maximum gradient. Mean (line) and standard deviation (shaded area) of 30 realizations each. The vertical line marks the depth of the control line.

Evidently, the higher irregularity in the MP heterogeneity model as compared to the MG model is consistent with the increased hydraulic non-equilibrium. The CB model, in turn, does not evoke changes in front irregularity, as far as

the variability in locations of maximum hydraulic head gradient is concerned. For a better understanding of a potential causal link between front spreading and hydraulic non-equilibrium, some insights on their relation might be helpful. To this end, we compare them in Fig. 4.11.

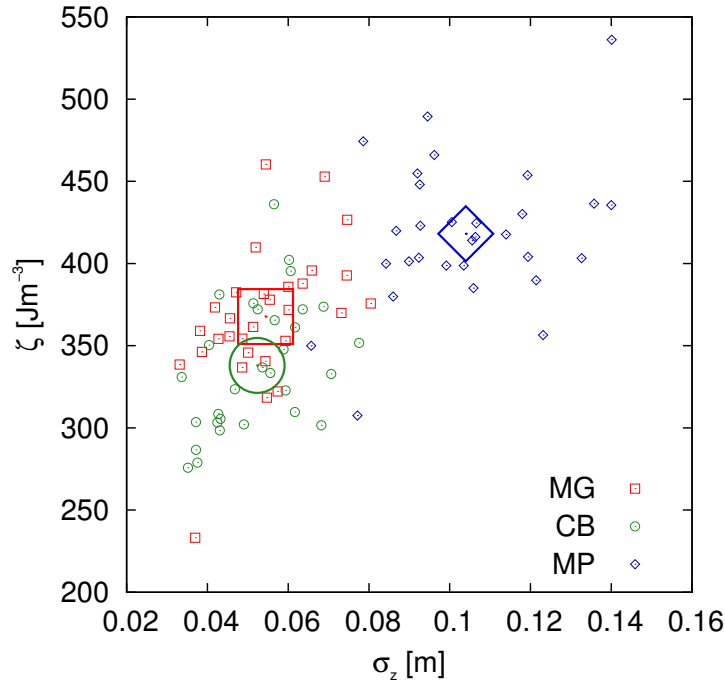


Figure 4.11: Comparison between hydraulic non-equilibrium and front irregularity for every realization. Big symbols represent averages. Notation is according to the last figures.

Figure 4.11 confirms the general agreement between the spatial and hydraulic aspect of non-equilibrium. Both are affected towards the same direction by connectivity modifications. However, the trend is not linear. Moreover, there is a considerable amount of noise in the data that may stem from too short travel distances or from an improper choice of non-equilibrium and front morphology estimators.

4.3.4 Time-dependency of hydraulic non-equilibrium

For this reason we set up some additional statistics on hydraulic and spatial non-equilibrium, which have a special focus on the time-dependency of non-equilibrium. Fig. 3.10 suggests that front irregularity is not perfectly normal distributed around a given mean depth. In that case higher moments than

just σ_z may carry some additional information. Another robust measure on front irregularity is the fraction of pixels along the control line, that have already been traversed by the front. Furthermore, the enclosed area between the dynamic and equilibrium water characteristic in Fig. 3.13 is substituted by the time-dependent difference in flux-weighted pressure head and the static counterpart $\langle h_m \rangle_j - h_m^{\text{eq}}(\langle \theta \rangle)$ at the given saturation $\langle \theta \rangle$ or the deviation of dynamic saturation from equilibrium saturation $\langle \theta \rangle - \theta^{\text{eq}}(\langle h_m \rangle_j)$ at the given pressure head $\langle h_m \rangle$. In Fig. 3.13 they correspond to vertical and horizontal distances, respectively. These additional statistics are compared in Fig. 4.12.

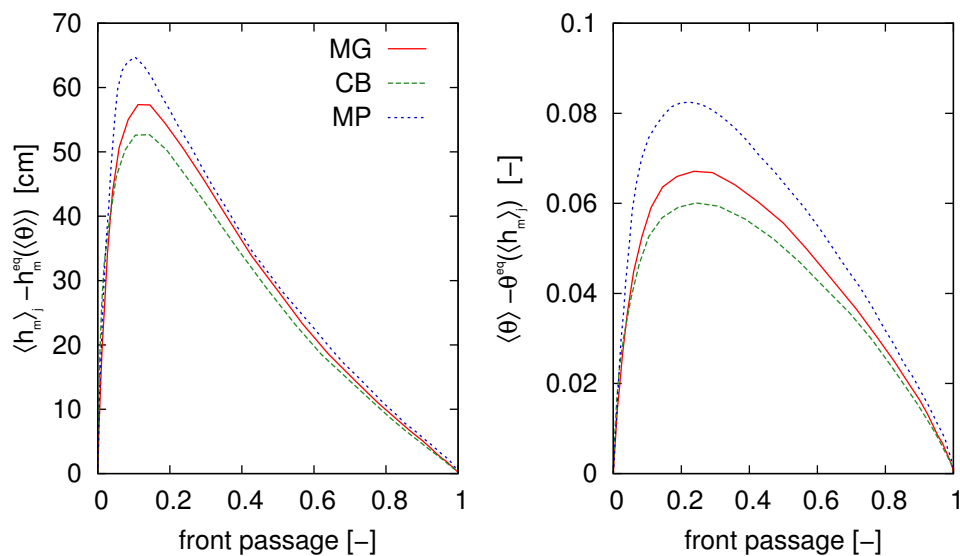


Figure 4.12: Evolution of the deviation of dynamic pressures (left) and dynamic water contents (right) from an equilibrium state as a function of the proportion of the control line that has already been traversed by the front. Lines represent mean values of 30 realizations each. Notation is according to the last figures.

The left figure illustrates the distinct two-stage behavior in the evolution of dynamic pressure heads at hydraulic non-equilibrium. First, there is a quick excursion of flux-weighted pressure heads, that is caused by a small percentage of the front, more precisely the first tip arriving at the given depth. At the second stage an almost linear relaxation towards equilibrium sets in. The maximum pressure deviation occurs at equal shares for all heterogeneity models, indicating that the width of the fastest advancing channel of the front is similar. Seemingly, the fraction at which the peak occurs depends on the correlation length and the heterogeneity of Miller medium σ_χ which are equal for all

heterogeneity models, but not on the connectivity. Yet, the maximum pressure excursion is different for MG, CB and MP. This points out to a higher degree of funneling and thus a different concentration of flux in equally narrow channels. The evolution of non-equilibrium saturation is depicted on the right hand side of Fig. 4.12. Evidently, the shape is also skewed but the transition of the two stages is smoother. In the CB model saturation non-equilibrium is lowest due to the highest density of high-flux channels and the lateral redistribution of water therein.

Chapter 5

Discussion

5.1 Structural connectivity as a concept

In Chapter 1 the question has been raised, what minimum amount of morphological description is required to capture structural connectivity in a representative way, so that it facilitates the prediction of effective hydraulic behavior in heterogeneous structures. By means of stochastic reconstruction it has been tested, whether local metrics that measure connectivity over short ranges are already sufficient to reproduce structural connectivity of the entire structure. The success depend strongly on the specific metric:

The autocovariance function reflects the correlation between two distant points in a heterogeneous field and does not address possible connections between them. As a consequence, there is virtually an infinite number of configurations without a connection between distant points and only a few "ordered" configurations where a connected path exists (Journel and Deutsch, 1993). Only in a very special case, namely the Multigaussian heterogeneity model, spatial correlation happens to coincide with structural connectivity because the long-range connectivity of high-K zones is at minimum.

Minkowski functions are obtained from pixel configurations in a 2×2 pixel neighborhood. As a consequence, any spatial feature outreaching this compact neighborhood is not captured. Although the Euler number of high-K zones, their area fraction and their boundary length with the background is reproduced for every level set, connectivity of high-K zones over long ranges does

not arise as an emergent property. Again, this is because the probability of a disordered pattern of clusters in a purely random structure is overwhelming.

A corrective in this regard is to consider chord length distributions. Thereby, the thickness of high-K zones is reproduced along four principal directions (horizontal, vertical, $2\times$ diagonal). However, this is only informative, when these zones exhibit a (i) compact, convex shape or (ii) a rather artificial morphology of a straight, concave pattern aligned to the principal directions. This is not fulfilled by the connected high-K bands in the CB heterogeneity model since they are concave and rather curvilinear. Hence, reproducing the chord length distribution of the foreground phase only, does not suffice to reproduce structural connectivity. However, if one assesses the chord length distribution of the background phase, some valuable information is achieved. This is because a higher degree of structural connectivity inevitably leads to a higher fragmentation of the background phase irrespective the morphology of the high-K zones.

Finally, the combination of Minkowski functions and chord length distributions results in the best reproduction of structural connectivity. This becomes especially evident for the CB structure at level sets close to the percolation threshold and has been demonstrated by means of local percolation probability and mean connectivity lengths. This is because the information content of both metrics is complementary: chord length distributions provide information on local attributes, in particular the fragmentation of the background phase by local clustering of high-K zones, whereas Minkowski functions additionally shape the structure by enforcing global mean attributes like the overall boundary length with the background and the global topology of the foreground in terms of Euler numbers.

However, even this combined multi-point statistics did not result in a perfect reproduction of structural connectivity. The reason for this shortcoming is depicted in Figure 5.1. The level set images demonstrate that the elongated bands in the reconstructed CB structures are not as continuous as in the reference CB structure. The reconstructed bands are interrupted at some points so that the connectivity of clusters is impaired and percolation probability of high-K zones is reduced. Figure 5.1 also depicts the improved resemblance of shape attributes of the bands by additional optimization of Minkowski functions in

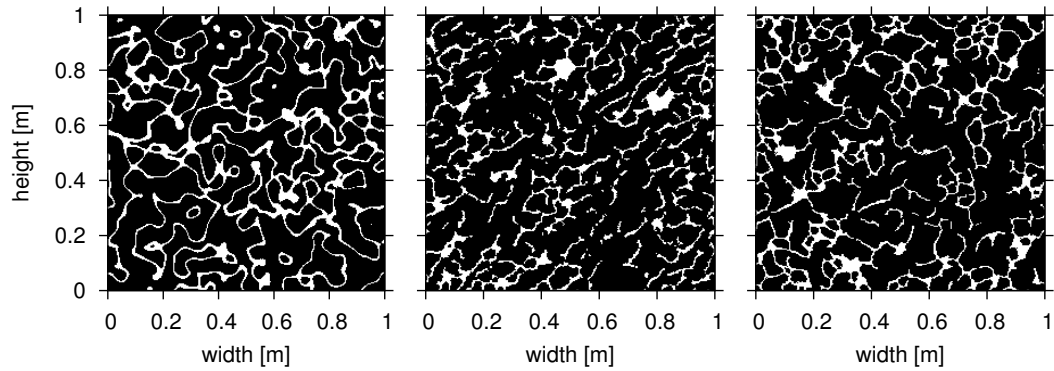


Figure 5.1: Level set of the reference (left) and reconstructed CB structures (cl-middle, mp-right) thresholded at the percolation threshold of the reference structure

the combined mp heterogeneity model as compared to the cl heterogeneity model only.

From these results some conclusions can be drawn. First, a combination of different multi-point statistics is necessary to thoroughly describe the connectivity of a complex structure. Secondly, local connectivity metrics may suffice to reproduce structural connectivity in random structures in a computationally effective way, if one is willing to accept a minor reduction of connectivity due to small gaps. Essentially, this also implies that structural connectivity is an emergent property of the entire domain that describes how the local morphology of structures affects the existence of continuous paths over long ranges. Recent studies have demonstrated that even further improvement in reproduction of structural connectivity is possible, yet with the disadvantage of higher computational cost. For instance, the pair connectivity function, also denoted as two-point cluster function, can be reconstructed directly by means of a complex upgrading scheme (Jiao et al., 2009). A simplified approach is to utilize it indirectly as a control statistic for readjustment of reconstruction parameters (Čapek et al., 2009). Another avenue is to abandon structural connectivity metrics completely and focus on the direct reproduction of patterns (Okabe and Blunt, 2005; Mariethoz et al., 2010). In essence, this equals the optimization of pixel configurations as it is done for Minkowski functions, yet within much larger neighborhoods.

5.2 Relation between structural and functional connectivity metrics

The motivation of this thesis has been the hypothesis that structural connectivity is an important feature of spatial heterogeneity that governs the effective hydraulic behavior of the subsurface. Consequently, one objective of this work has been to explore the causal links how differences in structural connectivity evoke differences in functional connectivity. The hydraulic behavior of the reconstructed heterogeneity models is especially suited to examine these relationships. In general, the results for steady-state flow and solute transport corroborate the causal link between structural and functional connectivity. It turns out that a good reproduction of structural connectivity also results in a good reproduction of hydraulic behavior. Likewise, a poor reproduction also entails a mismatch in indicators of functional connectivity. For the MG heterogeneity model the low connectivity of high-K zones could be reproduced easily by all structural connectivity metrics, which also resulted in a good fit of effective hydraulic conductivity and solute arrival times. For the CB heterogeneity model with high connectivity of high-K zones an improved reproduction of structural connectivity resulted in an improved reproduction of preferential flow and early solute arrival. The small gaps between high-K clusters that impaired a perfect reproduction of structural connectivity also entail a reduction in effective conductivity, whereas transport conductivity remains almost unaffected. One possible interpretation is that the evolution of flow networks in heterogeneous media is not solely determined by structural percolation properties. In addition the heterogeneous pressure field tends to bridge local spots of reduced conductivity by increasing the local head gradients. Hence, the overall flux patterns does not change as compared to an imaginary field without these gaps, which is why transport connectivity remains rather unaffected. This is in line with the findings of Knudby and Carrera (2006), suggesting that transport connectivity is less affected by the continuity of highly conductive channels but more sensitive to other shape attributes like the width of these channels, which is identical for the reference and reconstructed images.

5.3 Critique on flux-weighted pressure heads

The second numerical experiment examined the influence of structural connectivity on transient hydraulic behavior during infiltration with particular regard to effective hydraulic non-equilibrium. This is achieved by flux-weighted averaging of pressure heads, which conserves hydraulic non-equilibrium during upscaling. This is because the flux-weighted pressure head integrates spatial variations in local pressure heads and spatial variations in local water fluxes. Flux-weighted averages of pressure heads can be used to set up a dynamic water characteristic, where the averaged pressure head and water content in a given control volume decouple at the infiltration front (Vogel et al., 2010a).

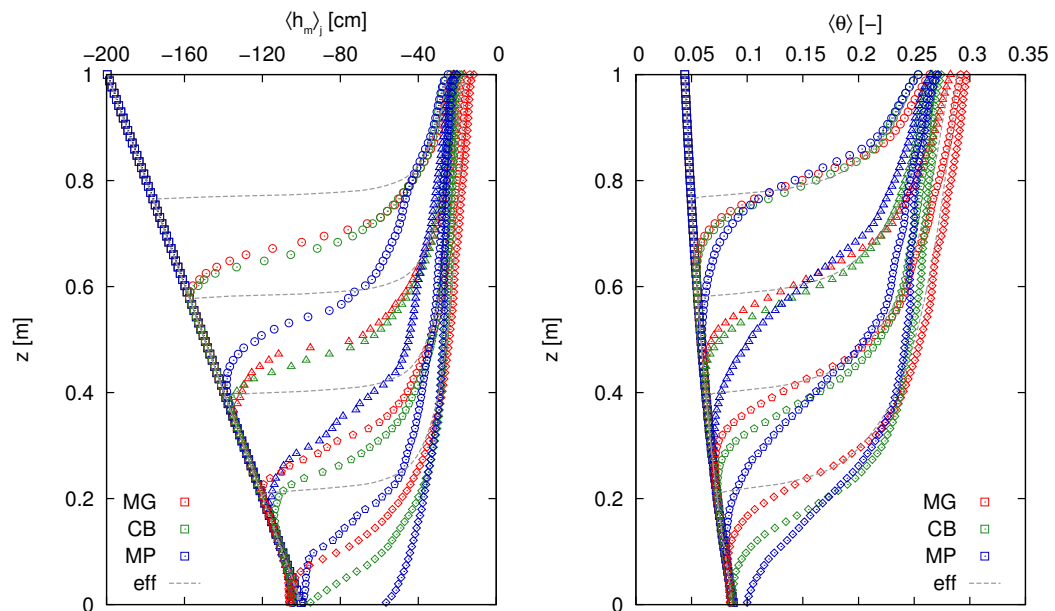


Figure 5.2: Vertical profile of averaged pressure heads $\langle h_m \rangle_j$ (left) and averaged water contents $\langle \theta \rangle$ (right) for three different heterogeneity models at 0 h (squares), 0.5 h (circles), 1 h (triangles), 1.5 h (pentagons) and 2 h (rhombs). Symbols represent mean values of 30 realizations each. Grey lines represents a homogeneous material with effective parametrization.

This decoupling is nicely reflected by the averaged 1D infiltration profiles in Figure 5.2. Apparently, the infiltration front advances faster with respect to pressure heads as compared to water contents. This effect is in line experimental observations (Topp et al., 1967; Vachaud et al., 1972; Wildenschild et al., 2001). Moreover, Figure 5.2 again stresses the impact of structural connectiv-

ity on the speed of the infiltration front and the final saturation behind the front. The decoupling of averaged state variables comprises two distinct processes: a quick excursion from equilibrium water retention curve followed by a gradual relaxation towards a new equilibrium under steady-state conditions. That is to say, there is one configuration of local state variables that can be achieved rapidly given the spatial structure of the material, and another one that corresponds to the energetic optimum. This corresponds to the initial excitation leading to hydraulic non-equilibrium followed by a relaxation towards the equilibrium conditions. The decoupling of water content and pressure head during non-equilibrium has been introduced by Ross and Smettem (2000) who suggested a simple linear kinetic of the water content towards equilibration:

$$\partial_t \theta = -\frac{\theta - \theta^{eq}}{\tau} \quad (5.1)$$

where θ and θ^{eq} are the dynamic and equilibrium water content and τ is a relaxation parameter. This derivative describes an instantaneous onset of non-equilibrium and an exponential relaxation in time towards a new equilibrium saturation. Figure 5.3 demonstrates that this behavior is actually not true for this simulated infiltration study. Both, dynamic pressure heads and dynamic water contents show a formation of non-equilibrium which is not instantaneous but evolving in time with almost the same rates as the relaxation to equilibrium afterwards. The relaxation is more parabolic than exponential. This discrepancy has two reasons: (i) The linear kinetic in eq. 5.1 does not claim general validity, but was rather chosen for its simplicity and because it reproduced field observations quite well (Ross and Smettem, 2000). (ii) Using Richards equation restrains hydraulic non-equilibrium in comparison to natural conditions. In reality, dynamic effects of moving interfaces at the pore scale might evoke an additional decoupling of h_m and θ (Schultze et al., 1999; Wildenschild et al., 2001, 2005; Weller et al., 2011) that reinforces qualitatively different non-equilibrium dynamics.

Apparent drawbacks of flux-weighted pressure heads are that (i) the weighting factor is not a scalar but a vector and that (ii) the average becomes ill-defined under complete no-flow conditions. Both are not critical. Since (i) the interest normally lies in an adequate representation of water dynamics with an 1D-effective model, we take only the directional component into account

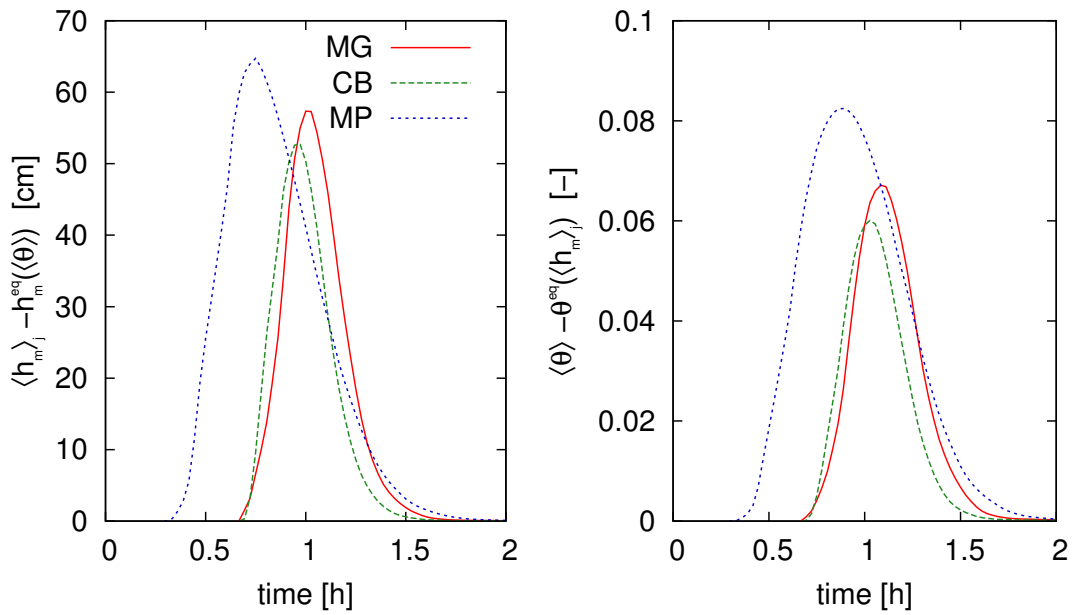


Figure 5.3: Evolution of the deviation of dynamic pressures (left) and dynamic water contents (right) from an equilibrium state as a function of time for different heterogeneity models (MG - Multigaussian, CB - connected bands, MP - macropores). Lines represent mean values of 30 realizations each.

that is oriented in the direction of the 1D-model (normally vertical). Furthermore, (ii) under static conditions hydraulic heads are constant everywhere in the horizontal plane and the equilibrium water retention curve is valid. In summary, flux-weighted averaging of pressure heads is a promising approach to effectively describe hydraulic behavior in heterogeneous soils under highly transient flow conditions. Obtaining the necessary information from field observations is not feasible with current technology. However, its application in numerical experiments may help to improve the model kinetics as originally proposed by Ross and Smettem (2000) and ultimately to couple the kinetics with structural parameters.

5.4 Impact of connectivity on hydraulic non-equilibrium

At first sight the results presented with respect to connectivity are quite contradictory. Even though the long-range connectivity of high-K zones is increased

in the CB and the MP model as compared to the standard MG heterogeneity model the MP model causes an enhancement in hydraulic non-equilibrium, whereas the CB heterogeneity model tends to reduce it. Evidently, the difference in the spatial arrangement of high-K zones evokes this opposite trend. In the CB model the increased lateral redistribution of water due to a higher lateral connectivity smooths front irregularities and reduces hydraulic non-equilibrium. This is in line with (Knudby and Carrera, 2006), who examined the same heterogeneity model and elaborated a causal link between structural connectivity and apparent diffusivity. The extreme anisotropy of the high-K channels in the macropore model instead, enforces concentration of flux in a few channels with high continuity (Le Goc et al., 2010), which evokes a distinct non-equilibrium behavior. The question is, how these findings relate to natural conditions. In real soil anisotropy of macropores with a strong vertical orientation is rather the rule than the exception, as they are typically composed of root channels and earthworm burrows. A fast movement of water in macropores that bypasses the soil matrix is extensively studied in literature (Jarvis, 2007; Clothier et al., 2008; Köhne et al., 2009) and also denoted as a preferential flow. The results presented here confirm an increased hydraulic non-equilibrium due to preferential flow in macropores and provide new means to quantify it.

5.5 Relation between functional connectivity metrics

For a final comment on the relationship between flow, transport and non-equilibrium connectivity metrics the numerical experiment on stationary single phase flow and transport of a conservative tracer is also carried out for the MP heterogeneity model. The indicators of functional connectivity are compared in Figure 5.4.

First of all, the different amount of scatter in the data demonstrates that a representative elementary volume (REV) (Bear, 1972) strongly depends on the process and the underlying structure. The coefficient of variation is similar for the MG and CB heterogeneity model for all processes considered and increases from CF ($CV_{MG} = 0.030$, $CV_{CB} = 0.039$) to CT ($CV_{MG} = 0.062$,

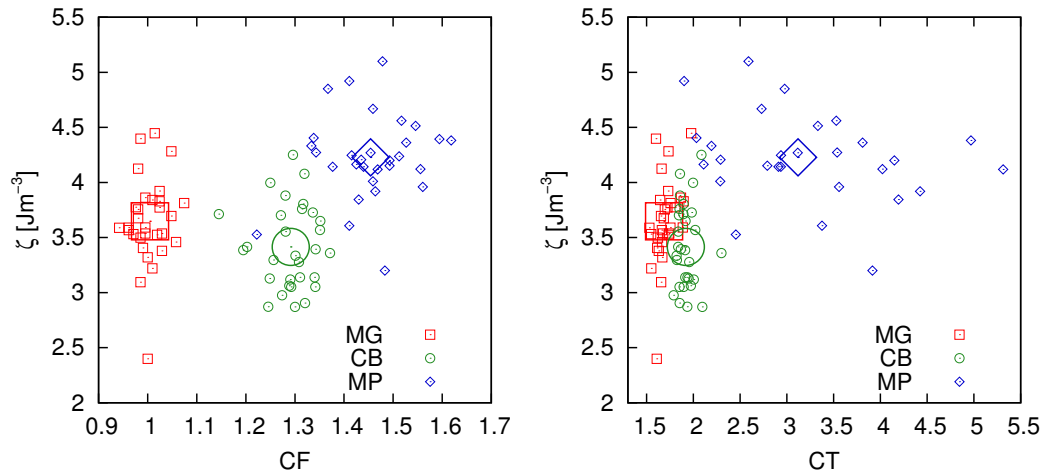


Figure 5.4: Comparison of effective hydraulic non-equilibrium and effective saturated conductivity via ζ and CF (left) and effective solute spreading via CT (right) for the MG, CB and MP model.

$CV_{CB} = 0.054$) and is highest for ζ ($CV_{MG} = 0.108$, $CV_{CB} = 0.110$) because it is measured after a shorter distance. The macropores in the MP heterogeneity enhance the variation only slightly for flow ($CV_{MP} = 0.058$) but considerably for transport ($CV_{MP} = 0.495$), whereas for ζ it is even slightly reduced ($CV_{MP} = 0.092$) in comparison to the other heterogeneity models.

Secondly, the fact that the MP heterogeneity model enhances all three functional connectivity metrics, whereas the CB heterogeneity model does not, corroborates previous findings that functional connectivity is a process and state-dependent concept (Knudby and Carrera, 2005, 2006; Renard and Al-lard, 2011).

Chapter 6

Conclusions

6.1 What constitutes structural connectivity?

Spatial heterogeneity of soils has many facets. One of them is the spatial connectivity of highly conductive zones within the soil. The objective of this work has been to find some meaningful metrics of structural connectivity that facilitate the prediction of effective hydraulic behavior. In order to do so, several local metrics that capture the amount of short-range connectivity by different means (autocovariance, Minkowski functions, chord length distribution) have been used to reproduce two different reference heterogeneity models (Multi-gaussian heterogeneity, connected bands heterogeneity) by means of stochastic reconstruction. The success of reproduction has then been validated by other metrics that capture the structural connectivity of the entire structure (local percolation probability, pair connectivity function).

It turns out that an increase in short-range connectivity of high-K zones indeed entails an improvement of structural connectivity over long ranges. In other words, long-range structural connectivity in stochastic structures emerges from the local morphology of high-K clusters. It was demonstrated that the combination of chord length distributions and Minkowski functions is a promising means to measure structural connectivity at low computational cost. This is because the two metrics provide complementary information: the first measures the local morphology of clusters whereas the second measures their global topology and regularity. A shortcoming of these combined multi-point statistics are some small gaps in the connected bands heterogene-

ity model that can be detected and removed by more complex connectivity metrics that measure long-range connectivity directly at higher computational cost.

Strictly speaking, this conclusion is only valid for the investigated set of random structures. As far as deterministic structures are considered, a long-range connectivity is not necessarily linked to short-range connectivity. This has been demonstrated by the macropore heterogeneity model. Structural features in natural porous media are not random but evolve from deterministic processes. These processes tend to produce patterns in which the high-K zones like root channels, earthworm burrows or gravel lenses persist over long distances but may establish only poorly connected networks.

6.2 What governs functional connectivity?

The predictive power of a structural connectivity metric on effective hydraulic behavior is only assured, when it captures those features of a complex structure that actually govern the specific process. That is to say, differences in effective hydraulic behavior must be linked to a comparable difference in a structural connectivity metric assuming equality in all other space, material and process attributes, whereas equal effective hydraulic behavior has to come along with equal values of structural connectivity metric. This causal link has proved true for steady-state flow and transport of a conservative tracer in random porous media. Here, equal structural connectivity of the reference Multigaussian heterogeneity model and its stochastically reconstructed counterparts entail equal indicator values of flow and transport connectivity for the two models. Moreover, for the connected bands heterogeneity model a difference in structural connectivity between the reference and the reconstructions evoke also a difference in flow and transport connectivity. However, both are not affected to the same degree. This is because flow connectivity is more sensitive to the continuity of high-K zones, whereas transport connectivity is more sensitive to general spatial arrangement of the flux field.

The numerical experiment on hydraulic non-equilibrium during infiltration clearly falsified a simple causal link between structural and functional connectivity. Here, effective hydraulic non-equilibrium serves as a functional con-

nectivity metric that quantifies the deviation between dynamic and static water retention due to preferential flow. It turns out that differences in structural connectivity might either reduce or enhance hydraulic non-equilibrium depending on a delicate balance of downward and lateral flux components. Infiltration into connected bands tends to reduce non-equilibrium because the omni-directional channels allow for higher lateral flux and a quick depletion in head gradients in a horizontal control volume. Isolated, vertically oriented macropores, however, enforce hydraulic non-equilibrium, because the flux is concentrated in a few anisotropic channels and lateral equilibration is reduced. Here emerges an apparent inconsistency: the increased structural connectivity in the MP heterogeneity model as compared to the Multigaussian reference leads to an increase in all investigated functional connectivity metrics, whereas in the CB heterogeneity model it does not. This is an additional evidence that functional connectivity is a process and state-dependent concept (Knudby and Carrera, 2005, 2006; Renard and Allard, 2011).

6.3 Outlook

In this thesis the impact of connectivity on soil hydraulic behavior has been investigated by theoretical considerations and numerical simulations. An important question remains: How can real world applications benefit from these findings. That is to say, how can we incorporate connectivity into soil hydraulic modeling? To begin with, is it necessary at all? There are some plausible scenarios, when structural connectivity is not important for the hydraulic behavior of a pedon, an agricultural plot or even an entire catchment. First of all, this includes situations in which the subsurface is only weakly heterogeneous. Secondly, there are subsurface bodies in which the structural connectivity of a feature of interest, say preferential flow paths or low-K barriers, is low, due to its small volume fraction or its actual morphology. In these situations some conservative assumption on spatial heterogeneity may suffice to predict hydraulic behavior. Note, however, that structural features in soil often stem from deterministic processes, like sedimentation, desiccation, biological activity, etc., which in fact tend to produce connected structures. Thirdly, even in the presence of high structural connectivity, the soil can be

in a state in which the features of interest are not active. For instance, after a small rain event a previously dry topsoil typically remains unsaturated and macropores do not contribute to flow. Thus, their structural connectivity does not affect infiltration. Same applies to upward flow during evaporation.

In summary, connectivity is important when (i) the soil heterogeneity is at a level at which the spatial arrangement of subsurface features starts to impact effective behavior and (ii) the soil hydraulic conditions favor this impact. In these occasions incorporation of connectivity into soil hydraulic modeling may improve model predictions. Then, a feasible strategy for a quantitative assessment of connectivity is to gather information at a two different scales (Vogel and Roth, 2003; Vereecken et al., 2007; Renard and Allard, 2011). At the small scale many soil cores can be collected in order to measure physical properties in the lab and many small-scale field experiments can be performed at different locations for a statistical evaluation of soil heterogeneity that facilitates a prediction of effective hydraulic behavior. At a larger scale the actual, effective hydraulic behavior (e.g. tile drain outflow, groundwater level changes, contaminant breakthrough) is monitored. Both sources of information can be compared and interpreted towards functional connectivity metrics. This strategy already permits a decision on which heterogeneity models can be excluded because of a mismatch between predictions and observations as it has been demonstrated in groundwater studies (Kerrou et al., 2008; Fernández-García et al., 2010; Bianchi et al., 2011). However, it does not allow for an exact localization of spatial features. Ideally, functional connectivity metrics could be used directly to condition a stochastic model of structural connectivity by distributed measurements and hydraulic tomography. However, some additional information to condition a representative model of the subsurface can be gathered with less effort. This comprises the interpretation of existing soil survey data and representative soil profiles at the site (Hammel et al., 1999; Deurer et al., 2001; Coquet et al., 2005; Vogel et al., 2006), but also a direct measurement of structural heterogeneity in soil by means of geophysical measurements at the field scale (Vereecken et al., 2004; Rubin and Hubbard, 2005).

A promising perspective provided by this study is a new conceptual model of hydraulic non-equilibrium in soil. With dynamic averaging of state variables

1D effective non-equilibrium behavior can be modeled under rapidly changing boundary conditions through decoupling of water content and pressure heads. It has been briefly described how the approach of Ross and Smettem (2000) to incorporate non-equilibrium dynamics into Richards equation could possibly be improved. The next step is to really compare that improved 1D model with the 2D numerical results along the lines of Vogel et al. (2010a). However, some open questions remain, e.g. the definition of a non-equilibrium conductivity term. Moreover, the introduction of a new conceptual model calls for a comparison with other established, conceptual non-equilibrium water flow models (two-domain, dual-permeability, etc.) to stress its benefits and drawbacks. Yet, this is certainly out of scope of this thesis.

Appendix A

Functional normalization

The frequency distribution of scaling factors along the control line of each realization is not perfectly log-normal. Therefore, the average water content at the line $\langle\theta\rangle_{\text{line}}$ for a given $\langle\psi_m\rangle_j$ does not coincide with the effective water retention curve of the entire domain even under hydrostatic conditions or at hydrodynamic equilibrium. As a consequence, the start and convergence point of the dynamic water retention curve do not superimpose with the equilibrium curve so that the integration limits for hydraulic non-equilibrium are ill-defined. This problem can be resolved by functional normalization.

Functional normalization is typically applied to coalesce many experimental observations of ψ_m and θ measured at a set of soil samples into a single water retention curve (Nielsen et al., 1998; Vereecken et al., 2007). The reference retention curve is determined by least square regression analysis. That is, the reference hydraulic parameters and a specific scaling factor χ for every sample has to be determined by an optimization algorithm. In a numerical experiment, however, the reference water retention curve is already known from the beginning. Thus, a normalized, average water content $\langle\theta\rangle_{\text{norm}}$ can be easily obtained by (i) applying Eq. 2.1 with the reference parametrization $(n, \alpha, \theta_r, \theta_s)$ to every local matric potential $\psi_{m,i}$ along the control line and (ii) calculating the arithmetic mean of these local, normalized water contents:

$$\frac{\langle\theta\rangle_{\text{norm}} - \theta_r}{\theta_s - \theta_r} = \frac{1}{n} \sum_i^n \{1 + [\alpha|\psi_{m,i}|]^n\}^{-1+1/n} \quad (\text{A.1})$$

where i is the location identifier and n is the amount of all pixels along the control line. However, the objective is not to coincide with the reference water

retention curve, but with the effective water retention curve of the entire Miller medium. Hence, α and n have to be substituted by the effective parameters $\langle\alpha\rangle$ and $\langle n\rangle$. Thus the modified equation reads

$$\frac{\langle\theta\rangle_{\text{eff}} - \theta_r}{\theta_s - \theta_r} = \frac{1}{n} \sum_i^n \left\{ 1 + [\langle\alpha\rangle |\psi_{m,i}|]^{\langle n\rangle} \right\}^{-1+1/\langle n\rangle} \quad (\text{A.2})$$

These effective parameters $\langle\alpha\rangle$ and $\langle n\rangle$ have to be determined beforehand, by (i) calculating effective water contents for the entire Miller medium $\langle\theta(\psi_m)\rangle$ for many ψ_m and (ii) fitting an instance of Eq. 2.1 to the data by applying a standard optimization algorithm, e.g. Levenberg-Marquardt (Press et al., 1992).

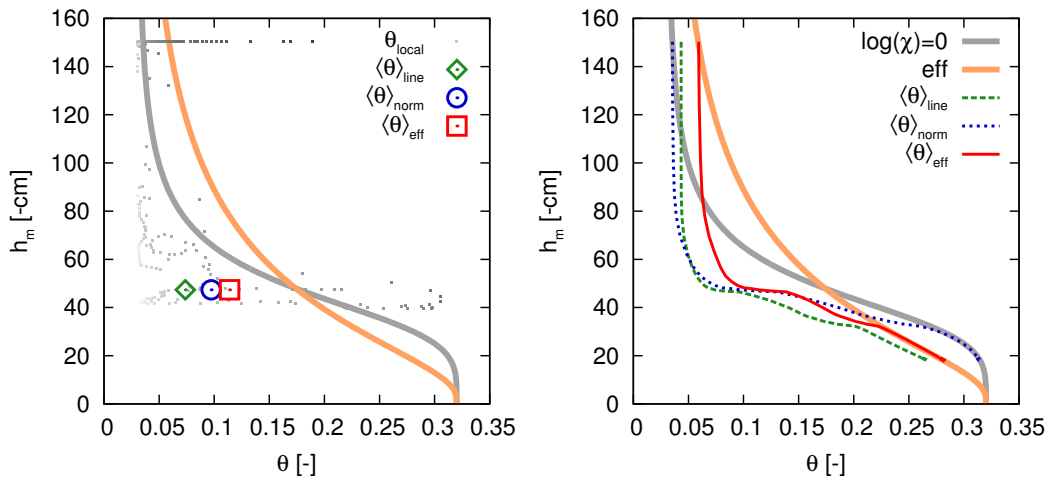


Figure A.1: Functional renormalization of averaged water contents at a horizontal control line for the MG heterogeneity model in Fig. 3.1. $\langle\theta\rangle_{\text{line}}$, $\langle\theta\rangle_{\text{norm}}$ and $\langle\theta\rangle_{\text{eff}}$ are the original and normalized averages of water content at the control line after 70 min (left) or for the entire experiment (right).

Figure A.1 demonstrates the performance of functional normalization. The $\langle\theta\rangle - \langle\psi_m\rangle$ trajectories on the right hand side show that the integration limits for effective hydraulic non-equilibrium ζ become clearly defined again by functional normalization. The snapshot at 70 min on the left hand side illustrates that solely $\langle\theta\rangle$ is rescaled while $\langle\psi_m\rangle_j$ remains unaffected.

Bibliography

- Allard, D., HERESIM Group, 1993. Geostatistics Tróia 92. Vol. 1. Kluwer Academic Publishers, Ch. On the connectivity of two random set models: the truncated Gaussian and Boolean, pp. 467–478.
- Antoine, M., Javaux, M., Bielders, C., 2009. What indicators can capture runoff-relevant connectivity properties of the micro-topography at the plot scale? *Advances in Water Resources* 32, 1297–1310.
- Bakr, A., Gelhar, L., Gutjahr, A., MacMillan, J., 1978. Stochastic analysis of spatial variability in subsurface flows: 1. Comparison of one-and three-dimensional flows. *Water Resources Research* 14 (2), 263–271.
- Bear, J., 1972. *Dynamic of fluids in porous media*. Elsevier, New York.
- Besag, J., Green, P., Higdon, D., Mengersen, K., 1995. Bayesian Computation and Stochastic Systems. *Statistical Science* 10, 3–66.
- Beven, K., Germann, P., 1982. Macropores and Water Flow in Soils. *Water Resources Research* 18 (5), 1311–1325.
- Bianchi, M., Zheng, C., Wilson, C., Tick, G., Liu, G., Gorelick, S., 2011. Spatial connectivity in a highly heterogeneous aquifer: From cores to preferential flow paths. *Water Resources Research* 47 (5), W05524, 3.
- Carle, S., Fogg, G., 1997. Modeling Spatial Variability with One and Multidimensional Continuous-Lag Markov Chains. *Mathematical Geology* 29.
- Clothier, B., Green, S., Deurer, M., 2008. Preferential flow and transport in soil: progress and prognosis. *European Journal of Soil Science* 59 (1), 2–13.

- Coquet, Y., Coutadeur, C., Labat, C., Vachier, P., van Genuchten, M., Roger-Estrade, J., Simunek, J., 2005. Water and solute transport in a cultivated silt loam soil: 1. Field observations. *Vadose Zone Journal* 4 (3), 573.
- Dagan, G., 1986. *Statistical Theory of Groundwater Flow and Transport: Pore to Laboratory, Laboratory to Formation and Formation to Regional Scale*. *Water Resources Research* 22, 120–134.
- Dagan, G., 1989. *Flow and transport in porous formations*. Vol. 465. Springer-Verlag New York.
- de Marsily, G., Delay, F., Goncalves, J., Renard, P., Teles, V., Violette, S., 2005. Dealing with spatial heterogeneity. *Hydrogeology Journal* 13, 161–183.
- de Rooij, G., 2011. Averaged water potentials in soil water and groundwater, and their connection to menisci in soil pores, field-scale flow phenomena, and simple groundwater flows. *Hydrology and Earth System Sciences* 15, 1601–1614.
- Delhomme, J., 1979. Spatial variability and uncertainty in groundwater flow parameters: a geostatistical approach. *Water Resources Research* 15 (2), 269–280.
- Deurer, M., Duijnsveld, W. H. M., Böttcher, J., 2001. Heterogeneous solute flow in a sandy soil under a pine forest: evaluation of a modelling concept. *Journal of Plant Nutrition and Soil Science* 164, 601–610.
- Deutsch, C., Journel, A., 1998. *GSLIB Geostatistical Software Library and User's Guide*, Applied Geostatistics, 2nd Edition. Oxford University Press, New York.
- Fernández-García, D., Trinchero, P., Sanchez-Vila, X., 2010. Conditional stochastic mapping of transport connectivity. *Water Resources Research* 46, W10515.
- Flury, M., Flühler, H., Jury, W., Leuenberger, J., 1994. Susceptibility of soils to preferential flow of water: A field study. *Water Resources Research* 30 (7), 1945–1954.

- Fogg, G., 1986. Groundwater flow and sand body interconnectedness in a thick, multiple-aquifer system. *Water Resources Research* 22 (5), 679–694.
- Freeze, R., 1975. A stochastic-conceptual analysis of one-dimensional groundwater flow in nonuniform homogeneous media. *Water Resources Research* 11 (5), 725–741.
- Gelhar, L., 1986. *Stochastic Subsurface Hydrology - From Theory to Applications*. *Water Resources Research* 22, 135–145.
- Gelhar, L., 1993. *Stochastic Subsurface Hydrology*. Prentice Hall, Old Tappan, NJ.
- Ghodrati, M., Jury, W., 1992. A field study of the effects of soil structure and irrigation method on preferential flow of pesticides in unsaturated soil. *Journal of contaminant Hydrology* 11 (1-2), 101–125.
- Gómez-Hernández, J., Wen, X., 1997. To be or not to be multi-Gaussian? A reflection on stochastic hydrogeology. *Advances in Water Resources* 21, 47–61.
- Goovaerts, P., 1997. *Geostatistics for Natural Resources Evaluation*. Oxford University Press.
- Gray, W., 2002. On the definition and derivatives of macroscale energy for the description of multiphase systems. *Advances in Water Resources* 25, 1091–1104.
- Hammel, K., Gross, J., Wessolek, G., Roth, K., 1999. Two-dimensional simulation of bromide transport in a heterogeneous field soil with transient unsaturated flow. *European Journal of Soil Science* 50 (4), 633–647.
- Harvey, C., Gorelick, S., 2000. Rate-limited mass transfer or macrodispersion: Which dominates plume evolution at the macrodispersion experiment (MADE) site? *Water Resources Research* 36 (3), 637–650.
- Hendrickx, J., Flury, M., 2001. Uniform and preferential flow, mechanisms in the vadose zone, conceptual models of flow and transport in the fractured vadose zone. National Research Council, National Academy Press: Washington, DC.

- Hilfer, R., 2002. Review on Scale Dependent Characterization of the Microstructure of Porous Media. *Transport in Porous Media* 46, 373–390.
- Hillel, D., 1998. *Environmental soil physics*. Academic Press, San Diego.
- Hunt, A., 2001. Applications of percolation theory to porous media with distributed local conductances. *Advances in Water Resources* 24, 279–307.
- Ippisch, O., Vogel, H.-J., Bastian, P., 2006. Validity limits for the van Genuchten-Mualem model and implications for parameter estimation and numerical simulation. *Advances in Water Resources* 29, 1780–1789.
- Jarvis, N. J., 2007. A review of non-equilibrium water flow and solute transport in soil macropores: principles, controlling factors and consequences for water quality. *European Journal of Soil Science* 58, 523–546.
- Jiao, Y., Stillinger, F., Torquato, S., 2009. A superior descriptor of random textures and its predictive capacity. *Proceedings of the National Academy of Science* 106 (42), 17634–17639.
- Journel, A., Alabert, F., 1989. Non-Gaussian data expansion in the Earth Sciences. *Terra Nova* 1, 123–134.
- Journel, A., Deutsch, C., 1993. Entropy and spatial disorder. *Mathematical Geology* 25 (3), 329–355.
- Kerrou, J., Renard, P., Hendricks Franssen, H., Lunati, I., 2008. Issues in characterizing heterogeneity and connectivity in non-multiGaussian media. *Advances in Water Resources* 31 (1), 147–159.
- Kirkpatrick, S., Gelatt, C., Vecchi, M., 1983. Optimization by Simulated Annealing. *Science* 220 (4598), 671–680.
- Kleidon, A., Schymanski, S., 2008. Thermodynamics and optimality of the water budget on land: a review. *Geophysical Research Letters* 35, L20404.
- Knudby, C., Carrera, J., 2005. On the relationship between indicators of geo-statistical, flow and transport connectivity. *Advances in Water Resources* 28, 405–421.

- Knudby, C., Carrera, J., 2006. On the use of apparent hydraulic diffusivity as an indicator of connectivity. *Journal of Hydrology* 329, 377–389.
- Köhne, J., Köhne, S., Simunek, J., 2009. A review of model applications for structured soils: a) Water flow and tracer transport. *Journal of Contaminant Hydrology* 104, 4–35.
- Koltermann, C., Gorelick, S., 1996. Heterogeneity in sedimentary deposits: A review of structure-imitating, process-imitating, and descriptive approaches. *Water Resources Research* 32, 2617–2658.
- Korteland, S., Bottero, S., Hassanizadeh, S., Berentsen, C., 2009. What is the Correct Definition of Average Pressure? *Transport in Porous Media* 84, 153–175, 3.
- LaBolle, E., Fogg, G., 2001. Role of molecular diffusion in contaminant migration and recovery in an alluvial aquifer system. *Transport in Porous Media* 42 (1), 155–179.
- Le Goc, R., de Dreuzy, J. R., Davy, P., 2010. Statistical characteristics of flow as indicators of channeling in heterogeneous porous and fractured media. *Advances in Water Resources* 33 (3), 257–269.
- Mantoglou, A., Gelhar, L., 1987. Large scale models of transient unsaturated flow systems. *Water Resources Research* 23 (1), 37–46.
- Mantz, H., Jacobs, K., Mecke, K., 2008. Utilizing Minkowski functionals for image analysis: a marching square algorithm. *Journal of Statistical Mechanics* P12015.
- Manwart, C., Torquato, S., Hilfer, R., 2000. Stochastic reconstruction of sandstones. *Physical Review E* 62, 893–899.
- Mariethoz, G., Renard, P., Straubhaar, J., 2010. The direct sampling method to perform multiple-point geostatistical simulations. *Water Resources Research* 46 (11), W11536.
- Matheron, G., 1967. *Eléments pour une théorie des milieux poreux*. Massion et Cie.

- Mecke, K., 2000. *Statistical Physics and Spatial Statistics The Art of Analyzing and Modeling Spatial Structures and Pattern Formation*. Vol. 554 of *Lecture Notes in Physics*. Springer, Ch. Additivity, Convexity and Beyond: Application of Minkowski Functionals in Statistical Physics, pp. 111–184.
- Mecke, K., Wagner, H., 1991. Euler Characteristic and Related Measures for Random Geometric Sets. *Journal of Statistical Mechanics* 64, 843–850.
- Metropolis, N., Rosenbluth, A., Rosenbluth, M., Teller, A., Teller, E., 1953. Equations of state calculations by fast computing machines. *Journal of Chemical Physics* 21, 1087–1091.
- Miller, E., Miller, R., 1956. Physical Theory for Capillary Flow Phenomena. *Journal of Applied Physics* 27, 324–332.
- Mualem, Y., 1976. Hysteretical models for prediction of the hydraulic conductivity of unsaturated porous media. *Water Resources Research* 12 (6), 1248–1254.
- Neuweiler, I., Cirpka, O., 2005. Homogenization of Richards equation in permeability fields with different connectivities. *Water Resources Research* 41, W02009.
- Neuweiler, I., Vogel, H.-J., 2007. Upscaling for unsaturated flow for non-Gaussian heterogeneous porous media. *Advances in Water Resources* 43.
- Nielsen, D., Hopmans, J., Reichardt, K., 1998. An emerging technology for scaling field oil-water behavior. Scale dependence and scale invariance in hydrology. Cambridge Univ. Press, Cambridge, UK, pp. 136–166.
- Ohser, J., Mücklich, P., 2000. *Statistical Analysis of Microstructures in Material Science*. Wiley & Sons, New York.
- Okabe, H., Blunt, M., 2005. Pore space reconstruction using multiple-point statistics. *Journal of Petroleum Science Engineering* 46, 121–137.
- Ouenes, A., Bhagavan, S., Bunge, P., Travis, B., 1994. Application of Simulated Annealing and Other Global Optimization Methods to Reservoir Description: Myths and Reality. In: *SPE 69th Annual Technical Conference and Exhibition*. New Orleans, pp. 547–561.

- Poeter, E., Townsend, P., 1994. Assessment of critical flow path for improved remediation management. *Ground Water* 32 (3), 439–447.
- Press, W., Teukolsky, S., Vetterling, W., Flannery, B., 1992. *Numerical Recipes in C: The Art of Scientific Computing*. Cambridge University Press.
- Renard, P., Allard, D., 2011. Connectivity metrics for subsurface flow and transport. *Advances in Water Resources*, in press.
- Renard, P., De Marsily, G., 1997. Calculating equivalent permeability: a review. *Advances in Water Resources* 20 (5), 253–278.
- Roberts, A., Torquato, S., 1999. Chord-distribution functions of three-dimensional random media: Approximate first-passage times of Gaussian processes. *Physical Review E* 59, 4953–4963.
- Robin, M., Gutjahr, A., Sudicky, E., Wilson, J., 1993. Cross-Correlated Random Field Generation With the Direct Fourier Transform Method. *Water Resources Research* 29 (7), 2385–2397.
- Ross, P., Smettem, K., 2000. A simple treatment of physical nonequilibrium water flow in soils. *Soil Science Society of America Journal* 64 (6), 1926–1930.
- Roth, K., 1995. Steady state flow in an unsaturated, two-dimensional, macroscopically homogeneous, Miller-similar medium. *Water Resources Research* 31 (9), 2127–2140.
- Roth, K., Hammel, K., 1996. Transport of conservative chemical through an unsaturated two-dimensional Miller-similar medium with steady state flow. *Water Resources Research* 32 (6), 1653–1663.
- Roth, K., Jury, W., Flühler, H., Attinger, W., 1991. Transport of chloride through an unsaturated field soil. *Water Resources Research* 27 (10), 2533–2541.
- Rubin, Y., 2003. *Applied stochastic hydrology*. Oxford University Press.
- Rubin, Y., Hubbard, S., 2005. *Hydrogeophysics*. Vol. 50 of *Water Science Technology Library*. Springer, Dordrecht.

- Samouëlian, A., Vogel, H.-J., Ippisch, O., 2007. Upscaling hydraulic conductivity based on the topology of the sub-scale structure. *Advances in Water Resources* 30, 1179–1189.
- Sánchez-Vila, X., Carrera, J., Girardi, J. P., 1996. Scale effects in transmissivity. *Journal of Hydrology* 183, 1–22.
- Schaap, J., Lehmann, P., Kaestner, A., Vontobel, P., Hassanein, R., Frei, G., de Rooij, G., Lehmann, E., Flühler, H., 2008. Measuring the effect of structural connectivity on the water dynamics in heterogeneous porous media using speedy neutron tomography. *Advances in Water Resources* 31 (9), 1233–1241, 3.
- Schultze, B., Ippisch, O., Huwe, B., Durner, W., 1999. Dynamic nonequilibrium during unsaturated water flow. In: *Proc. Int. Workshop: Characterization and Measurement of the Hydraulic Properties of Unsaturated Porous Media*, Riverside, CA. pp. 877–892.
- Shipitalo, M., Butt, K., 1999. Occupancy and geometrical properties of *Lumbricus terrestris* L. burrows affecting infiltration. *Pedobiologia* 43 (6), 782–794.
- Strebelle, S., 2002. Conditional Simulation of Complex Geological Structures Using Multiple-Point Statistics. *Mathematical Geology* 34, 1–21.
- Talukdar, M., Torsaeter, O., Ioannidis, M., Howard, J., 2002. Stochastic Reconstruction of Chalk from 2D Images. *Transport in Porous Media* 48, 101–123.
- Topp, G., Klute, A., Peters, D., 1967. Comparison of Water Content-Pressure Head Data Obtained by Equilibrium, Steady-State, and Unsteady-State Methods. *Soil Science Society of America Journal* 31 (3), 312–314.
- Torquato, S., Beasley, J., Chiew, Y., 1988. Two-point cluster function for continuum percolation. *Journal of Chemical Physics* 88 (10), 6540–6547.
- Čapek, P., Hejtmánek, V., Brabec, L., Zikánová, A., Kočířík, M., 2009. Stochastic Reconstruction of Particulate Media Using Simulated Annealing: Improving Pore Connectivity. *Transport in Porous Media* 76, 179–198.

- Vachaud, G., Vaudin, M., Wakil, M., 1972. A Study of the Uniqueness of the Soil Moisture Characteristic During Desorption by Vertical Drainage. *Soil Science Society of America Journal* 36 (3), 531–532.
- van Genuchten, M. T., 1980. A Closed-form Equation for Predicting the Hydraulic Conductivity of Unsaturated Soils. *Soil Science Society of America Journal* 44, 892–898.
- Vereecken, H., Hubbard, S., Binley, A., Ferré, T., 2004. Hydrogeophysics: An introduction from the guest editors. *Vadose Zone Journal* 3 (4), 1060.
- Vereecken, H., Kasteel, R., Vanderborght, J., Harter, T., 2007. Upscaling Hydraulic Properties and Soil Water Flow Processes in Heterogeneous Soils: A Review. *Vadose Zone Journal* 6, 1–28.
- Vogel, H.-J., 2000. A numerical experiment on pore size, pore connectivity, water retention, permeability, and solute transport using network models. *European Journal of Soil Science* 51 (1), 99–105.
- Vogel, H.-J., 2002. Topological characterization of porous media. *Morphology of Condensed Matter*. Springer, Heidelberg, pp. 75–92.
- Vogel, H.-J., Cousin, I., Ippisch, O., Bastian, P., 2006. The dominant role of structure for solute transport in soil: Experimental evidence and modelling of structure and transport in a field experiment. *Hydrology and Earth System Sciences* 2, 2153–2181.
- Vogel, H. J., Cousin, I., Roth, K., 2002. Quantification of pore structure and gas diffusion as a function of scale. *European Journal of Soil Science* 53 (3), 465–473.
- Vogel, H.-J., Roth, K., 2003. Moving through scales of flow and transport in soil. *Journal of Hydrology* 272, 95–106.
- Vogel, H.-J., Weller, U., Ippisch, O., 2010a. Non-equilibrium in soil hydraulic modelling. *Journal of Hydrology* 393, 20–28, 3.
- Vogel, H.-J., Weller, U., Schlüter, S., 2010b. Quantification of soil structure based on Minkowski functions. *Computers & Geosciences* 36 (10), 1236–1245.

- Vogel, T., Cislserova, M., Hopmans, J. W., 1991. Porous media with linearly variable hydraulic properties. *Water Resources Research* 27 (10), 2735–2741.
- Warrick, A., Mullen, G., Nielsen, D., 1977. Scaling field-measured soil hydraulic properties using a similar media concept. *Water Resources Research* 13 (2), 355–362.
- Weller, U., Ippisch, O., Köhne, M., Vogel, H.-J., 2011. Direct Measurement of Unsaturated Conductivity including Hydraulic Nonequilibrium and Hysteresis. *Vadose Zone Journal* 10 (2), 654.
- Wen, X., Gómez-Hernández, J., 1996. Upscaling hydraulic conductivities in heterogeneous media: An overview. *Journal of Hydrology* 183 (1-2), 9–23.
- Wen, X., Gómez-Hernández, J., 1998. Numerical modeling of macrodispersion in heterogeneous media: a comparison of multi-Gaussian and non-multi-Gaussian models. *Journal of Contaminant Hydrology* 30, 129–156.
- Western, A., Blöschl, G., Grayson, R., 2001. Toward capturing hydrologically significant connectivity in spatial patterns. *Water Resources Research* 37, 83–97.
- Whitaker, S., 1986. Flow in porous media I: A theoretical derivation of Darcy's law. *Transport in Porous Media* 1 (1), 3–25.
- Wildenschild, D., Hopmans, J., Rivers, M., Kent, A., 2005. Quantitative analysis of flow processes in a sand using synchrotron-based X-ray microtomography. *Vadose Zone Journal* 4 (1), 112, 1.
- Wildenschild, D., Hopmans, J. W., Simunek, J., Jan 2001. Flow Rate Dependence of Soil Hydraulic Characteristics. *Soil Science Society of America Journal* 65 (1), 35–48.
- Yeh, T. C. J., Gelhar, L. W., Gutjahr, A. L., 1985. Stochastic analysis of unsaturated flow in heterogeneous soils. 1. Statistically isotropic media. *Water Resources Research* 21 (4), 447–456.
- Yeong, C., Torquato, S., 1998. Reconstructing random media. *Physical Review E* 57, 495–505.

Zehe, E., Blume, T., Blöschl, G., 2010. The principle of maximum energy dissipation: a novel thermodynamic perspective on rapid water flow in connected soil structures. *Philosophical Transactions of the Royal Society B: Biological Sciences* 365 (1545), 1377–1386.

Zehe, E., Lee, H., Sivapalan, M., 2006. Dynamical process upscaling for deriving catchment scale state variables and constitutive relations for meso-scale process models. *Hydrology and Earth System Sciences* 10 (6), 981–996.

Zinn, B., Harvey, C., 2003. When good statistical models of aquifer heterogeneity go bad: A comparison of flow, dispersion, and mass transfer in connected and multivariate Gaussian hydraulic conductivity fields. *Water Resources Research* 39 (3), 1051.

Danksagung

Ein großer Dank gilt meinem Doktorvater und Mentor Prof. Dr. Hans-Jörg Vogel für die Überlassung des Themas, vor allem aber auch für die jahrelange, ausgezeichnete Betreuung und Förderung. Sein großer Erfahrungsschatz, sein wissenschaftliches Gespür und sein kreativer Input sind unschätzbar wertvolle Stützen für das Gelingen der Arbeit gewesen.

Ein großes Dankeschön möchte ich den Mitarbeitern des Departments Bodenphysik des UFZ's aussprechen, dessen offenes Arbeitsklima zu stetig neuen Ideen führt. Besonders bedanken möchte ich mich hier bei Dr. Ulrich Weller und Dr. John Maximilian Köhne für zahlreiche, anregende Diskussion und Hilfestellungen.

Diese Arbeit wurde vom Helmholtz-Vernetzungsfonds im Zuge des Virtuellen Instituts *Inverse Modelling of Terrestrial Systems - INVEST* finanziert. Unter den Projektpartnern möchte ich insbesondere Dr. Olaf Ippisch für seine geduldige Hilfe bei Softwarefragen und Prof. Dr. Jan Vanderborght für wichtige Anregungen bei methodischen Weiterentwicklungen danken.

Schließlich möchte ich meiner Freundin Ina-Maria von ganzen Herzen für ihre Unterstützung und Hingabe während der letzten drei aufopferungsvollen Jahre danken.

Eidesstattliche Erklärung

Hiermit erkläre ich, dass ich die vorliegende Arbeit selbständig und ohne fremde Hilfe verfasst, andere als die von mir angegebenen Quellen und Hilfsmittel nicht benutzt und die den benutzten Werken wörtlich oder inhaltlich entnommenen Stellen als solche kenntlich gemacht habe.

Halle (Saale), den 27.02.2012

Steffen Schlüter

Lebenslauf

Persönliche Daten

Name Steffen Schlüter
Geboren 23.03.1983 in Schlema
Familienstand ledig
Anschrift Schillerstr. 32, 06114 Halle (Saale)

Ausbildung

2004–2005 Auslandsaufenthalt an der Universität Sevilla (ERASMUS-Stipendium)
2002–2009 Studium der Geographie mit Nebenfachausbildung in Bodenkunde und Hydrologie an der Technischen Universität Dresden
2001–2002 Zivildienst am Helios-Klinikum in Aue
1993–2001 Abitur am J.-G.-Herder-Gymnasium in Schneeberg

Beruflicher Werdegang

seit 2009 Doktorand in der Arbeitsgruppe *Struktur und Funktion von Böden* des Departments Bodenphysik am Helmholtz-Zentrum für Umweltforschung - UFZ in Halle

Halle (Saale), den 27.02.2012

Steffen Schlüter